Quarterly Report for

Contract DE-FG36-02ID14418

Stanford Geothermal Program

October-December 2003

Table of Contents

1. EXPERIMENTAL STUDY OF RELATIVE PERMEABILITIES IN A FRACTURE

This project is being conducted by Research Assistant Chih-Ying Chen, Professor Roland Horne and Visiting Researcher Mostafa Fourar. In this research, an experimental apparatus was built to capture the unstable nature of the two-phase flow in a smooth-walled fracture and display the flow structures under different flow configurations in real time. The air-water relative permeability was obtained from experiment and showed deviation from the X-curve behavior suggested by earlier studies. Through this work, the relationship between the phase-channel morphology and relative permeability in fractures was determined. A phenomenological approach (tortuous-channel model) was proposed to quantify the effects of the flow structure. This approach could replicate the experimental results with a good accuracy. Other relative permeability models (viscous-coupling model, X-curve model and Corey-curve model) were also compared. Except for the viscous-coupling model, these models did not explain the experimental relative permeabilities as well as the proposed tortuous-channel model. Hence, we concluded that the two-phase relative permeability in fractures depends not only on liquid type and fracture geometry but also on the structure of the two-phase flow.

1.1 INTRODUCTION

Multiphase flows through fractured porous media are of great importance in several domains such as geothermal energy, petroleum recovery and environmental engineering. In the case of two-phase flow in a single fracture, this importance extends to several industrial processes such as compact heat exchanges and nuclear engineering. Despite this importance, few theoretical and experimental studies have been devoted to establishing the laws governing these flows. Thus, the results presented in the literature seem to be in contradiction. So far, the mechanisms of two-phase flows in a fracture are not well understood and a general model for describing these flows is still not determined.

The approach used commonly to describe two-phase flow in a fracture is the relative permeability concept, which is based on a generalization of the Darcy equation. Three models for the relative permeabilities are presented in the literature: the X-model (straight lines), the Corey model, and the viscous-coupling model. The experimental results presented in the literature also show different behavior for the relative permeabilities. Some results are in accordance with the X-model whereas other results are in accordance with the Corey-model or the viscous-coupling model.

Although the flow structures are of a great importance in modeling two-phase flows, the three models do not take these effects into account. The purpose of this research is to examine the effects of the flow structures on the relative permeabilities during two-phase flow in a single fracture.

1.2 BACKGROUND

In this section, we present the main theoretical models for relative permeabilities in a single fracture. Then, we discuss some experimental results from the literature.

1.2.1 Theoretical approaches

The equations used commonly to model steady-state laminar two-phase flow in a single fracture are the generalized Darcy equations:

$$u_l = \frac{k_{abs} k_{rl} (p_i - p_o)_l}{\mu_l L} \tag{1.1}$$

$$u_g = \frac{k_{abs} k_{rg} (p_i - p_o)_g}{\mu_g L} \tag{1.2}$$

where subscripts l and g stand for liquid and gas, respectively; p_i and p_o are the pressures at the inlet and the outlet of the fracture; u is the superficial velocity or the Darcy velocity (flow rate per unit of section area); μ is the dynamic viscosity; L is the fracture length; k_{abs} is the absolute permeability and k_{rl} and k_{rg} are the relative permeabilities of the liquid and the gas, respectively.

To take the compressibility effect of the gas into account, Equation 1.2 must be rewritten in the following form (Scheidegger, 1974):

$$u_g = \frac{k_{abs} k_{rg} (p_i^2 - p_o^2)}{2\mu_g L p_o} \tag{1.3}$$

The absolute permeability of a smooth-walled fracture is related to the fracture aperture, b, by (Yih, 1969: Eq. 341; Witherspoon et al., 1980):

$$k_{abs} = \frac{b^2}{12} \tag{1.4}$$

The concept of the relative permeability provides us a means to quantify the relative resistance or interference between phases. For liquid-gas flow, the sum of k_{rl} and k_{rg} indicates the extent of phase interference: the lower the sum of the relative permeabilities below 1, the greater the phase interference. The critical point of the generalized Darcy model is the determination of the relative permeabilities, which are usually supposed to be only functions of the saturation. When the pressure loss due to the interaction between phases is negligible against the pressure loss due to the flow of each fluid, the relative permeabilities can be modeled by the X-curves:

$$k_{rl} = S_l \tag{1.5}$$

$$k_{rg} = S_g \tag{1.6}$$

where S_l and S_g are the liquid and gas saturation respectively.

According to X-model, the sum of k_{rl} and k_{rg} equals 1, which means the absence of phase interference. Physically this implies that each phase flows in its own path without impeding the flow of the other. In fractures, if each phase flows via perfect straight channels along the flow direction with negligible capillary pressure and wetting-phase stratified flow, then X-curve behavior is possible. However, for two-phase flows through a real fracture, the surface contact between the two fluids can be important and, consequently, the interaction between the two fluids may not be negligible. As the fracture flow can be considered either as a limiting case of a flow in a porous medium (Pruess and Tsang, 1990) or as a limiting case of a pipe flow (Fourar et al., 1993), there are mainly two approaches for modeling relative permeabilities.

In the porous medium approach, the fracture is treated as a connected two-dimensional porous medium where the pore space occupied by one phase is not available for the flow of the other phase. A phase can move from one position to another only upon establishing a continuous flow path for itself. The competition for pore occupancy is controlled by the capillary pressure. Based on this approach, several numerical studies were performed (Murphy and Thomson, 1990; Rossen et Kumar 1994, Mondoza et Sudick, 1991, Pyrak-Nolte et al. 1992). The main result is that the sum of k_r is less than 1 and, consequently, the X-model is not suitable to describing the numerical calculations of the relative permeabilities as functions of the saturation. However, these studies did not establish theoretical relationships for k_r. The shape of the curves obtained was more similar to the curves obtained in classical porous media, namely the Corey curves (Corey, 1954):

$$k_{rl} = S^{*4} \tag{1.7}$$

$$k_{rg} = (1 - S^{*})^2 (1 - S^{*2}) \tag{1.8}$$

In these equations, S^{*} is the saturation defined by:

$$S^{*} = (S_l - S_{rl}) / (1 - S_{rl} - S_{rg}) \tag{1.9}$$

where subscript r refers to residual saturation. The Corey model represents strong phase-interference in comparison with the X-model.

The pipe flow approach is based on the observation that flow structures observed in a fracture show more similarity to the structures observed in a pipe than to those expected for a porous medium (Fourar and Bories, 1995). These flow structures show strong interference between the two fluids flowing simultaneously. However, the real mechanisms are very difficult to model because the geometry of the interface between the fluids is unknown and one of the phases is generally discontinuous. Fourar and Lenormand (1998) assumed that the complexity of the real flow can be modeled, in a first approximation, by viscous coupling between the fluids. The fracture is then modeled by two parallel planes

with a small aperture. The two fluids are flowing simultaneously and the interface is assumed to be planar. Fluid *l* is considered as the wetting fluid and therefore is in contact with the walls, and fluid *g* (nonwetting) flows in between. The viscous coupling between fluids is derived by integrating Stokes' equation for each stratum. Identification of the established equations and the generalized Darcy equations leads to:

$$k_{rl} = \frac{S_l^2}{2}(3 - S_l) \tag{1.10}$$

$$k_{rg} = (1 - S_l)^3 + \frac{3}{2}\mu_r S_l (1 - S_l)(2 - S_l) \tag{1.11}$$

where $\mu_r = \mu_g/\mu_l$ is the viscosity ratio.

These equations show that the relative permeability of the nonwetting fluid depends on the viscosity ratio μ_r. k_{rg} can be larger than unity when $\mu_r > 1$ (lubrication effects). However, for gas and liquid two-phase flows, $\mu_r << 1$ and, consequently, the second term in the right-hand-side of Equation 1.11 is negligible.

1.2.2 Experimental approaches

Several studies on two-phase flows in a fracture have been performed. Romm (1966) studied kerosene and water two-phase flow through an artificial fracture by using parallel glass plates. The surface of each plate was lined with strips of polyethylene or waxed paper. The strips divided the entire fracture into 10 to 20 narrow parallel fractures (2-3 mm width) with alternate wettability.

Persoff et al. (1991) and Persoff and Pruess (1995) also performed experiments on gas and water flow through rough-walled fractures using transparent casts of natural fractured rocks. The study of Persoff et al. (1991) showed strong phase interference similar to that in porous media. In these experiments, flow of a phase was characterized by having a localized continuous flow path that undergoes blocking and unblocking by the other phase.

Diomampo (2001) performed experiments of nitrogen and water flow through smooth-walled artificial fractures. She also observed the intermittent phenomenon in her experiments. Furthermore, her results conform mostly to the Corey type of relative permeability curve. This suggests that flow through fractures can be analyzed by treating it as a limiting case of porous media flow and by using the relative permeability approach.

Fourar et al. (1993) and Fourar and Bories (1995) studied air-water two-phase flow in a fracture constituted of two parallel glass plates (1.0 m x 0.5 m) with an opening equal to 1 mm. The injector consisted of 500 stainless steel tubes of 1 mm outside diameter and 0.66 mm inside diameter. Air and water were injected through alternating capillary tubes to achieve uniform distribution of the inlet flow. For all experiments, air was injected at a constant pressure and its volumetric flow rate was measured by a rotameter and corrected

to the standard pressure. Water was injected by a calibrated pump. At the outlet of the fracture, the gas escaped to the atmosphere and the water was collected.

The fracture was initially saturated with water, which was injected at a constant flow rate for each experiment. Air injection was then started and increased in steps. When the steady state was reached for each flow rate, the pressure drop and the saturation were measured. The pressure drop was measured by a transducer and the saturation was measured by using a balance method. Then, the fracture was resaturated with water and the experiment was repeated several times at different liquid flow rates. This study has been extended to fractures constituted by bricks made of baked clay (30 cm x 14 cm) with different apertures (0.54 mm, 0.40 mm and 0.18 mm).

Results obtained in these various studies are presented in Figure 1.1 in terms of k_{rg} versus k_{rl}. As can be seen, experimental results obtained by Romm (1966) are described well by the X-model, that is the relative permeability of each phase equals to its saturation. On the other hand, the relative permeablities obtained by Fourar and Bories (1995) are rather in accordance with the viscous-coupling model. However, the results obtained by Diomampo (2001) are described well by the Corey model. Lastly, the results obtained by Persoff and Pruess (1995) show more interaction between phases than the other results. It is obvious that these previous studies show a diversity of behavior of relative permeabilities in fractures. Furthermore, little attention has been paid to study the relationship between flow structures and relative permeabilities. Although the flow structure from the experimental study performed by Romm (1966) is not reported, it is likely that it was a channel flow due to the fracture configuration (alternate wetting and nonwetting stripes). In this case, the interaction between phases is minimum and, consequently, the results are described by the X-model. The experiments performed by Persoff et al. (1995) showed that the flow is characterized by having a localized continuous flow path that is undergoing blocking and unblocking by the other phase. This behavior is related to capillary effects, which are dominant in classical porous media. Consequently, the flow of one phase is strongly impeded by the flow of the other phase. In the experiments performed by Fourar and Bories (1995), several flow structures were observed: bubbles, fingering bubbles, drops and films. It seems that these flows are dominated by viscous forces.

The purpose of this study is to visualize and discuss the two-phase flow behavior in a fracture. The gas-water relative permeabilities obtained are analyzed by examining the flow structures. Finally a tortuous-channel approach is developed to reproduce experimental results and to show the effect of the flow structures on the relative permeabilities.

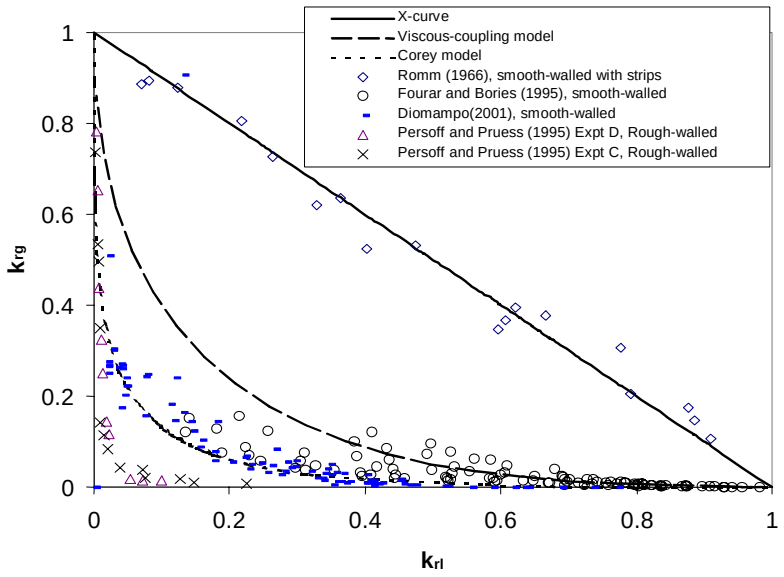

Figure 1.1: Compendium of previous measurements of relative permeabilities in fractures (Romm (1966) results from kerosene-water flow, the rest were air-water or nitrogen-water flow).

1.3 EXPERIMENTAL APPARATUS AND MEASUREMENTS

In this study, gas-water flow experiments were conducted at 24^{o}C. The fluids consisted of pure nitrogen and deionized water. The water injection was controlled by a meter pump (Dynamax, SD-200, rate: 0.1-200 ml/min). Gas injection was controlled through a flow regulator (Brooks Instrument, Flow Controller Model 0151E), which was connected to a gas meter (Brooks Instrument, Flow Meter model 5850E, max. rate: 200 ml/min). All measurements were electronic and digitized by using high-speed data acquisition system (DAQ; National Instrument, SCSI-1000 with PCI 6023E A/D board) and digital video recording system (Sony Digital-8 560X with Pinnacle Studio DV IEEE 1394 image capture card). The whole experimental system is illustrated in Figure 1.2, which shows the fluid supply, the fracture apparatus, data acquisition system, and digital image recording. In this section, we first describe the fracture apparatus. Then we describe the pressure, flow rates, saturation measurements, and data processing method.

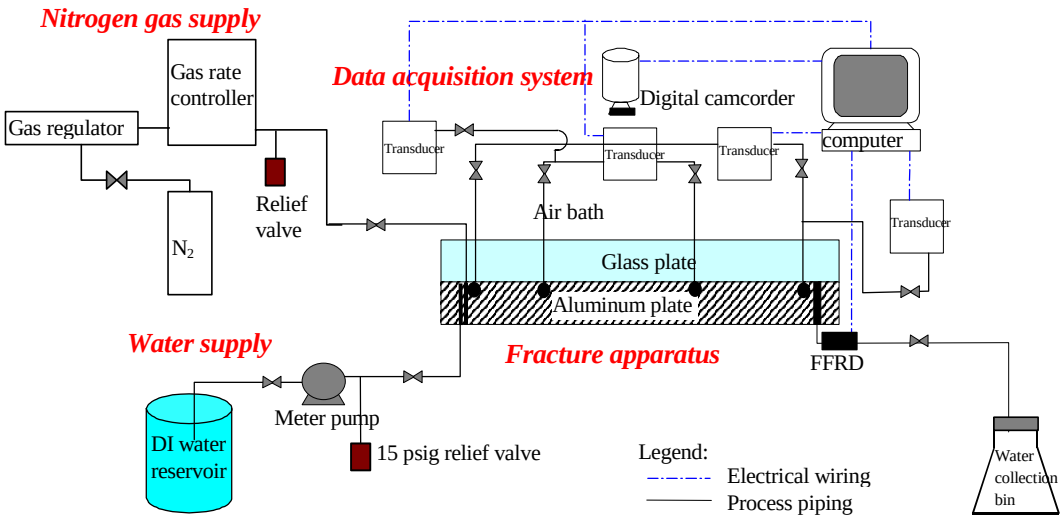

Figure 1.2: Process flow diagram for air-water experiment.

1.3.1 Fracture apparatus description

The fracture is created by a smooth glass plate on top of an aluminum plate confined by a metal frame bolted to the bottom plate. The aperture of the fracture was set to 130 μm by using stainless steel shims along the flow boundaries. The schematic view and photograph of the fracture apparatus are shown in Figure 1.3. An O-ring (Viton 1/8" thick #2-272) was placed in between the glass and aluminum plate as a seal. The fluids enter into the fracture through two separate canals. Each canal has several ports drilled in a way that they align on the surface (see Figure 1.3). The surface of the fracture apparatus was designed such that there is an available 12 inch by 4 inch space for flow. Throughout this flow area, tiny pressure ports were drilled so as to minimize surface discontinuity. Four pressure ports were drilled along the fracture as shown in Figure 1.3. The two-phase fluid exits through a single outlet. The apparatus was designed to be of sufficient length to minimize the capillary end effects.

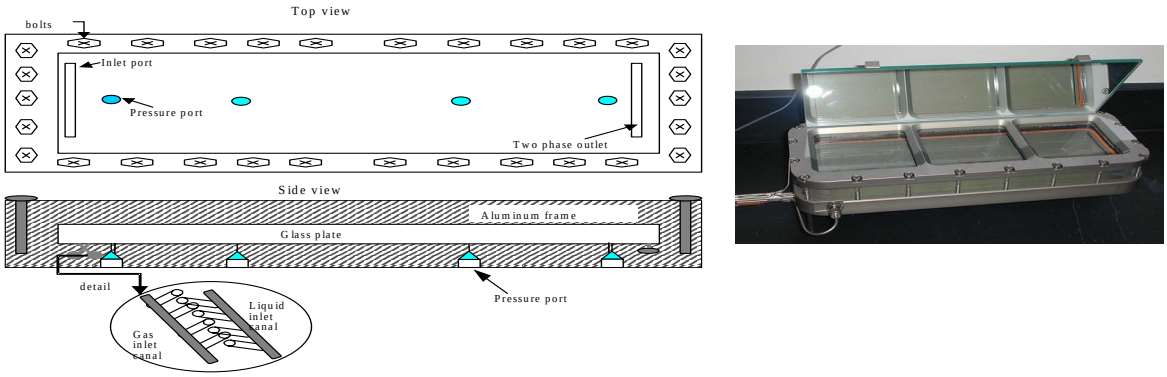

Figure 1.3: Schematic diagram and picture of fracture apparatus.

1.3.2 Pressure measurements

Low-range differential transducers were used to measure the pressure difference through the fracture, as well as the intermediate pressure and the two-phase outlet pressure. Two

liquid differential transducers (Validyne Transducer, model DP-15, range 0-2 psig) were attached to four pressure ports inside the fracture to measure the pressure difference through the fracture. Another transducer (Validyne Transducer, model DP-15, range 0-5 psig) was attached to the middle point of the fracture. The fourth transducer (Validyne Transducer, model DP-15, range 0-5 psig) was attached to the two-phase outlet of the fracture apparatus. These transducers send electrical signals to the data acquisition system, which was monitored using the LabView® programmable virtual instrument software. The complete measurement configuration in the fracture apparatus is shown in Figure 1.2.

1.3.3 Flow rates measurements

Aside from the known input rates, to obtain the instantaneous flow rates, a fractional flow ratio detector (FFRD) was designed and constructed as shown in Figure 1.4a. The FFRD was used to measure the outlet gas and water fractional flows, f_g and f_w.

$$f_g = \frac{q_{out,g}}{q_{out,t}} \quad \text{and} \quad f_w = \frac{q_{out,w}}{q_{out,t}} \tag{1.12}$$

$$q_{out,t} = q_{out,w} + q_{out,g} \tag{1.13}$$

where $q_{out,g}$ is the outlet gas flow rate, $q_{out,w}$ is the outlet water flow rate, and $q_{out,t}$ is the outlet total flow rate. The principle of the FFRD is that different phases will have different refractive indices. A phototransistor (NTE 3038, NPN-Si, Visible) was installed inside the FFRD, producing different voltages when sensing different strengths of light. The water phase produces a higher voltage when flowing through the FFRD as shown in Figure 1.4b. The gas and water phase flow ratios are obtained by determining the ratio of the number of gas and water signals. Once f_g and f_w are obtained at steady-state condition, it is easy to calculate $q_{out,g}$ in Equation 1.12 by assuming that water flow rate remains constant from inlet to outlet of the fracture. This assumption can hold if the wetting phase, water, flows in a continuous channel, and the water viscosity is much larger than the nonwetting phase. The calibration of the FFRD demonstrated a good linearity between measurement and actual values (Figure 1.5).

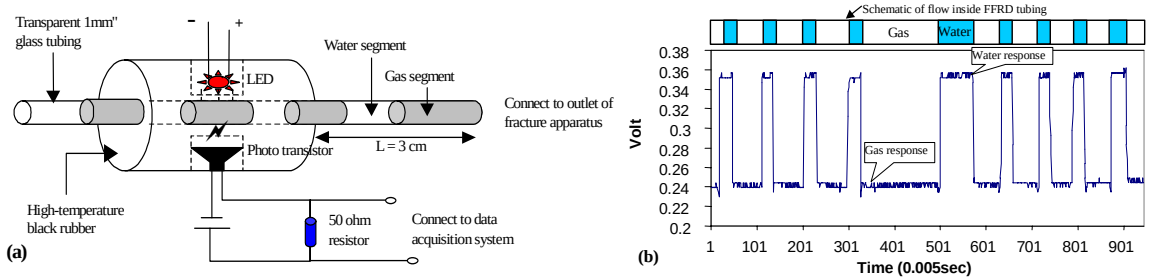

Figure 1.4: Fractional flow ratio detector (FFRD) (a) schematic (b) detected gas and water signal corresponding to different gas and water segments inside FFRD tubing.

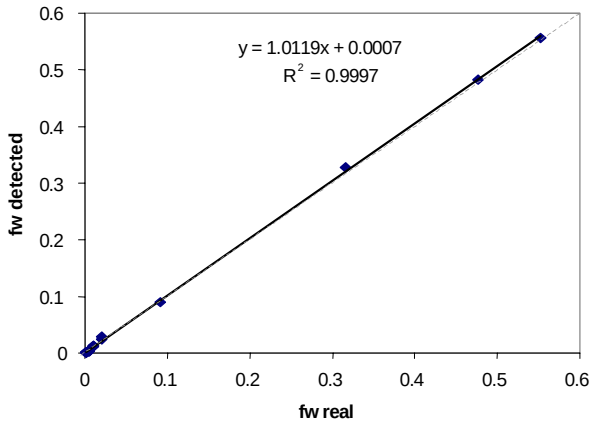

Figure 1.5: FFRD calibration (Fluids: water and nitrogen gas; FFRD tubing ID: 1.0mm).

1.3.4 Saturation measurements

Still images were extracted from digital video recorded during the experiments. The photographs were processed in a Matlab® program. The program does quadratic discriminant analysis (QDA) to divide the pixels of the picture into three groups: water phase, gas phase and the frame. The grouping is based on color differences. Saturation is calculated as total pixels of the liquid group over the sum of the gas and liquid groups. Figure 1.6 is a comparison of the gray-scaled image produced by the QDA program and the original photograph from the digital camcorder. Pan et al. (1996) also used a similar technique for measurement of saturation. Their study noted that the source of errors in this technique is the quality of the photographs and the water film adsorbed on the surfaces of the plates with the latter being of minimal effect. Good quality photographs are the ones with clear distinction between the gas and liquid phase. Good lighting is necessary so that the colors in the image come out clearly. The lighting should also be positioned in a way that it does not produce shadow on the flow area. The program will mistakenly take the shadow as gas phase even if there is liquid. From Figure 1.6, it can be said that the program has good accuracy.

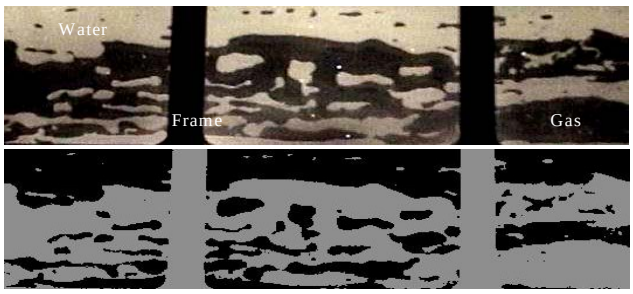

Figure 1.6: Comparison between the true color image of the fracture flow and gray scale image from the Matlab QDA program used in measuring saturation.

1.3.5 Data processing

The experiment was made in several runs with designated input rates of gas and water. According to the air-water experiments reported by earlier studies, these fracture flow experiments are not expected to reach a perfect steady state. Rather, they are unsteady by

nature. There are significant pressure fluctuations accompanied by saturation changes when the gas and liquid flow rates vary. Due to this behavior, instantaneous outlet rates of gas were also measured by the FFRD device for the relative permeability calculation and flow rate comparison. Digital video was taken in each run when the flow reached steady state or repeated similar fluctuating behaviors. The continuous images of each run were extracted from the video every 0.3 seconds. These hundreds of images in each run were then input into the computer programs for the saturation calculation, flow structure recognition and characterization of the stability of the two-phase flow. The data acquisition task requires frequent gathering of instantaneous and synchronized pressure, flow rate and saturation values. Instantaneous gathering of data was accomplished by the use of the high–speed data acquisition system and digital video camcorder. Video shots were taken of the pressure, time and saturation data displayed all at the same time. Pressure data and related time were displayed by the LCD monitor connected to the computer, which also ran the data acquisition system. The methodology used to integrate all the data and signals and then calculate the gas-water relative permeability is illustrated in the flow chart in Figure 1.7.

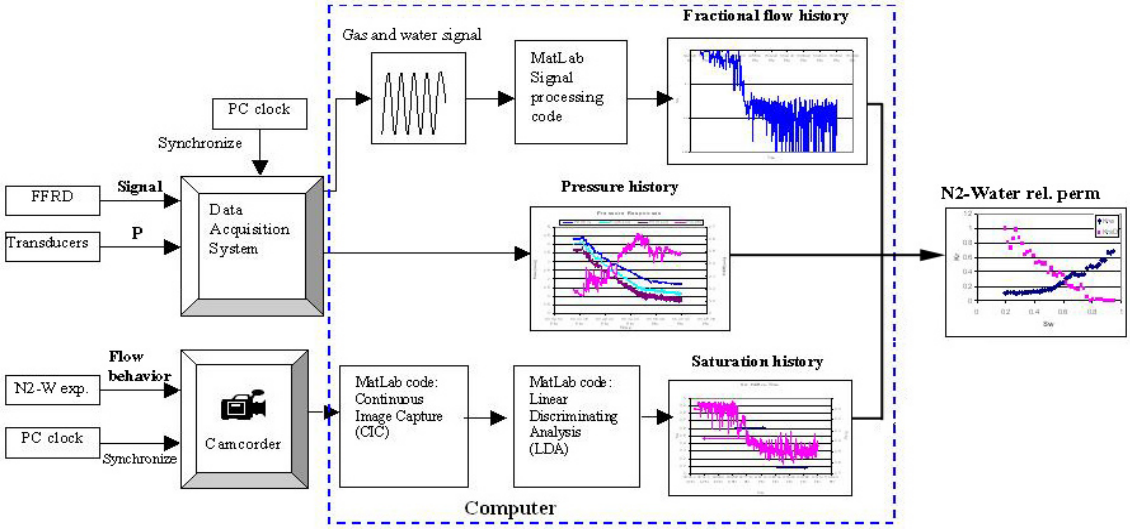

Figure 1.7: Data and signal processing flowchart.

1.4 EXPERIMENTAL RESULTS

We first describe the flow structures observed during the experiment, and then present the relative permeabilities calculated at one-second frequency in each run and their averaged values. Finally, we interpret the relative permeabilities using models from earlier studies.

1.4.1 Description of the flow structures

The use of a transparent glass plate allows us to observe and videotape the two-phase flow structures. The recorded digital video was then transformed to continuous snapshots with the frequency of 3 images/sec (0.33 seconds period). More than 3000 still images were extracted from the digital video and used for the flow structure characterization and saturation calculation. Several flow structures depending on the flow rates were observed.

Generally, when the water saturation decreases, one observes successively bubbles, slugs and channels (Figure 1.8).

The bubble flow is observed only at extremely high values of the water saturation, S_w. Due to the small fracture aperture (130 μm), large gas bubbles propagate either in bullet-like or ellipse-like forms with greater longitudinal length (Figure 1.8a). As the gas flow rate increases or water flow rate decreases, gas moves in narrow slugs and flows discontinuously when the gas rate is still relatively low as shown in Figure 1.8b. The higher pressure difference occurs mostly when a slug tries to break through the water region. Once the slug reaches the outlet of the fracture, the pressure difference decreases. This type of slug movement is seen frequently for high values of S_w. With the appearance of bubbles and slugs, the two-phase flow is fairly unstable. When the longitudinal size of slugs increases as the gas rate increases, the moving slugs tend to form stable gas channels and reach a steady condition. However, the steadiness collapses either because water breaks the thinnest throat of the short-lived channel or because of the insufficient gas supply. This causes continuous fluctuations in the saturation, fractional flow and pressure difference.

As the gas rate increases further, the short-lived channel becomes more and more stable. The gas channel meanders through the fracture with branches and junctions because the viscous force is insufficient to break through intermediate water islands. We define this kind of channel as a tortuous channel as shown in Figure 1.8c. The lifetime of these channels seems to depend on the complexity and meander of their structure. Some tortuous channels might exist just for a few seconds, whereas others exist for long periods. The S_w, f_w and pressure difference histories plotted in Figure 1.9 are obtained from a tortuous-channel-dominated run. Clearly, even though constant gas and water rates are injected into the fracture, the S_w keeps fluctuating in the fracture and the instantaneous f_w sensed from the FFRD follows this saturation fluctuation as shown in the top plot of Figure 1.9. The corresponding pressure response was also recorded as shown in the bottom plot of Figure 1.9. Most of the peaks in these two plots are due to the collapse, reconstruction and reconfiguration of channels, and some intrusions from other minor flow structures (bubbles and slugs). It is also observed that the more tortuous the channel, the larger the pressure difference along the fracture for the same water saturation.

On the other hand, straighter channels were observed more frequently in high f_g situations shown in Figure 1.8d. In this situation, almost all of the gas flows solely in a fairly straight channel, while most of the water flows above and below the gas path. Except for a small amount of immobile water inside the central gas channel, the gas path is more uniform and less tortuous in comparison with the tortuous channel flow. Three major factors may affect the morphology of gas channels. These factors are the f_g (viscous force), gas-water viscosity ratio (viscous force) and the interfacial tension (capillary force). Therefore for the same S_w, flows with the viscosity ratio closer to one or the smaller interfacial tension have straighter channels.

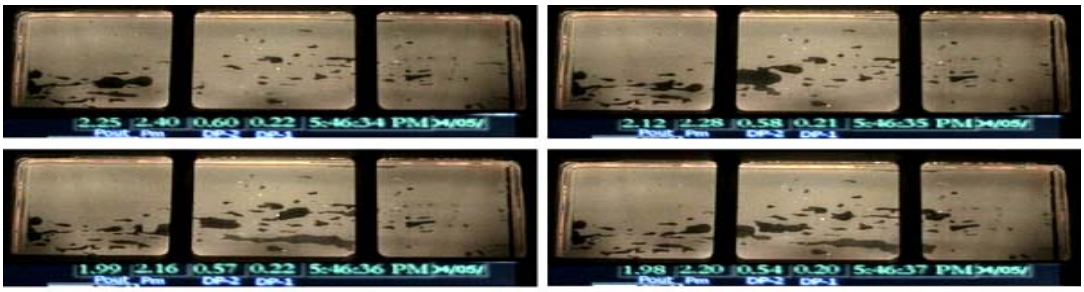

(a) Bubble Flow

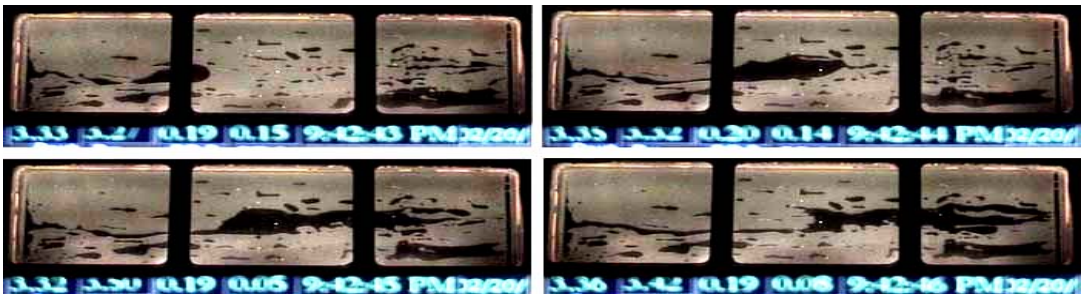

(b) Slug Flow

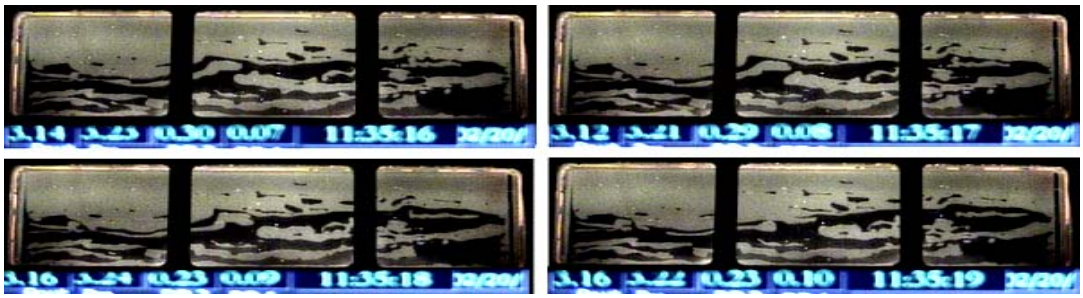

(c) Tortuous Channel Flow

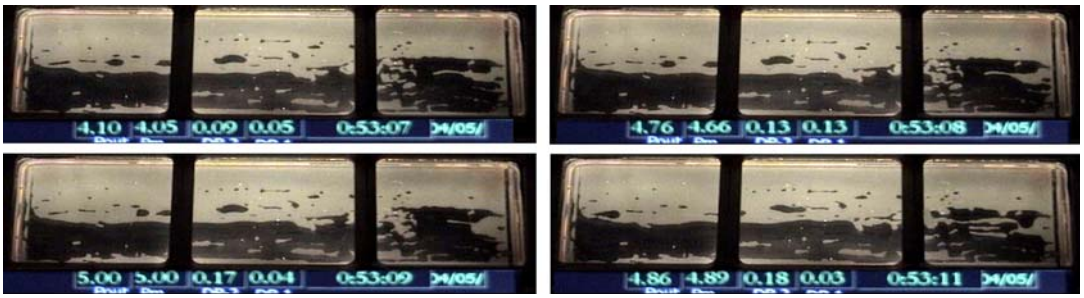

(d) Straight Channel Flow

Figure 1.8: Photographs of flow structures in the smooth-walled fracture. Each set contains four continuous images. Flow direction was from left to right.

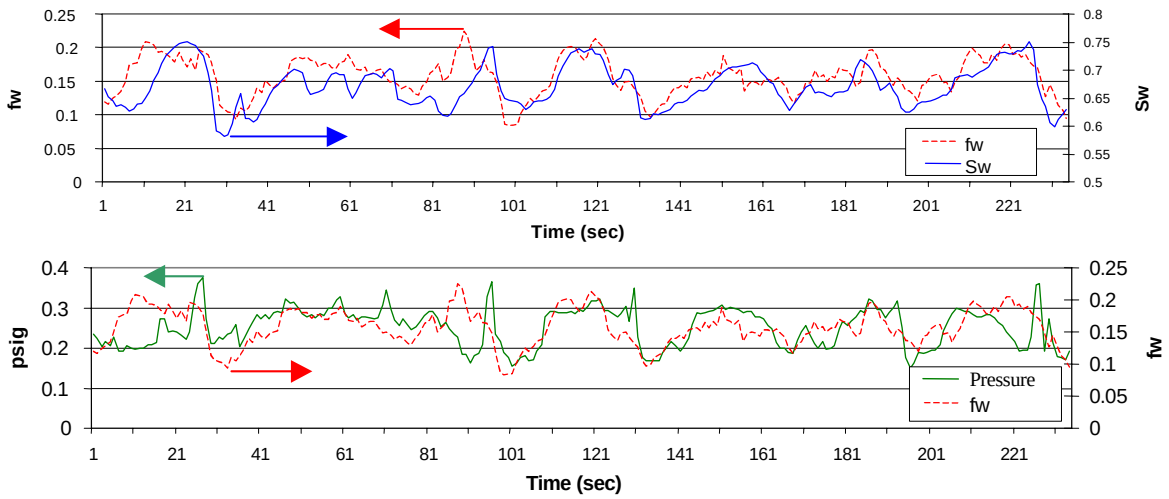

Figure 1.9: Relationship among water saturation (S_w), water fractional flow (f_w) and pressure difference along the fracture in a highly tortuous channel flow.

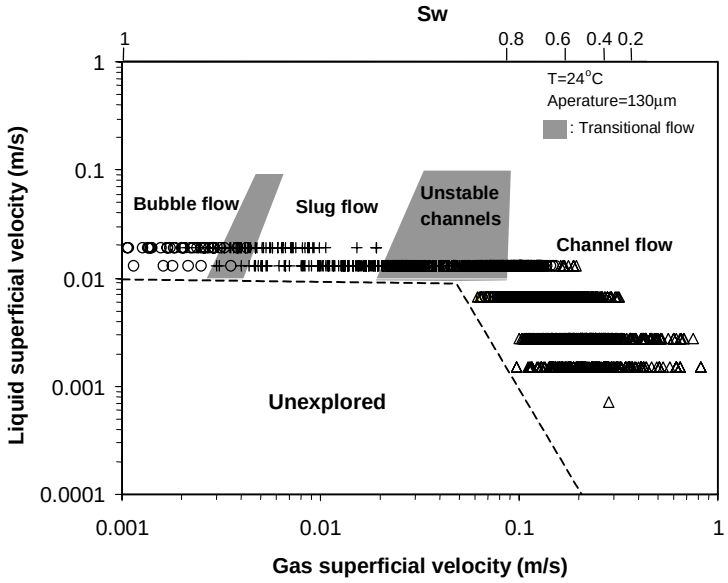

Figure 1.10: Flow structure map for air-water flow in the smooth-walled fracture.

Figure 1.10 shows a flow structure map for the experiment. The corresponding S_w is also provided in this figure. It is easy to see that the channel flow spans most of the S_w range and major bubble and slug flows only exist in high S_w situations. The shadow areas in the flow maps indicate transitional flow, which means the flow structure is a combination of the two neighboring structures. The transition between the slug flow and channel flow is defined as unstable channel flow. In this region, some large fingering slugs were able to bridge the two ends of the fracture. However, the bridged slug collapsed in a short time due to its unstable structure, water intrusion and the insufficient gas supply. The flow structure map is similar to the flow map (glass fracture) presented by Fourar and Bories (1995).

1.4.2 Relative permeability calculations

The absolute permeability of the smooth-walled fracture was first measured in single-phase water flow. The absolute permeability of the fracture deduced from measurements by using the Darcy equation is 1.51×10^{-9} m^2 (1510 darcies). The gap width (aperture) of the fracture is 130 μm, the estimated permeability from Equation 1.4 is then 1.41×10^{-9} m^2 (1410 darcies). As can be seen in Figure 1.11, measured values are in a good agreement with the theoretical value of the absolute permeability.

Air-water relative permeabilities were calculated by using Equations 1.1 and 1.3 at one-second frequency in each run. The instantaneous flow rate was obtained from the FFRD. Comprehensive air-water relative permeabilities obtained from thousands of data points are plotted in Figure 1.12. Data points in the figure show acceptable correlation. Comprehensive water relative permeabilities are scattered at high water saturation owing to the slug and unstable-channel flows in the gas-phase as shown in Figures 1.8a and 1.8b. The vertically scattered effect observed with the gas-phase relative permeability under extremely low values of water saturation may be associated with either the pressure fluctuation due to the moving water slugs or the difficulty in sensing the instantaneous f_w from the FFRD at low f_w.

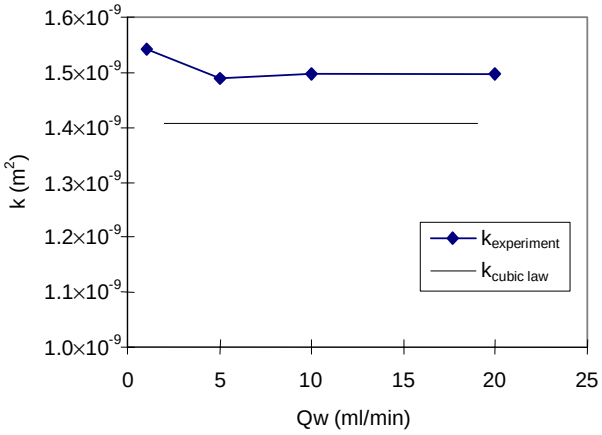

Figure 1.11: Absolute permeability of the fracture (aperture = 130 μm).

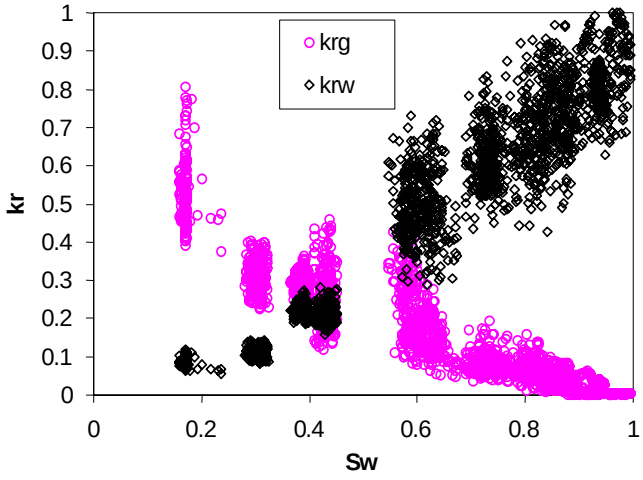

Figure 1.12: Comprehensive air-water relative permeabilities in the smooth-walled fracture.

1.4.3 Relative permeabilities interpretation

The averaged values of the relative permeabilities and the saturation for each pair of liquid and flow rates are presented in Figure 1.13. Also plotted in this figure are the curves of the X-model (Equations 1.5 and 1.6), the Corey-model (Equations 1.7 and 1.8) with $S_{rl} = 0$ and $S_{rg} = 0$, and the viscous-coupling model (Equations 1.10 and 1.11). It appears that the X-model does not fit the experimental data. For a given value of S_w, the k_{rl} and k_{rg} are below the straight lines. Although gas-phase experimental values are closer to the Corey curve, water-phase values are much higher than the water-phase Corey curve. Therefore, neither the Corey curve nor the X-curve can fit the experimental result. On the other hand, the viscous-coupling model is in agreement with experimental results, especially for the water-phase. For the gas phase, the viscous-coupling model shows acceptable fitting, but it seems to be less accurate at high water saturation. The photographs in Figure 1.8 provide some clue about this less accurate result. At high values of S_w, most of the water channels extend from longitudinal boundaries of the fracture space and flow straighter and more continuously. On the other hand, the active gas flows as fingering slugs and channels with amorphous shapes. These changing shapes generate the corresponding pressure, saturation and flow rate changes as illustrated in Figure 1.9. The relative permeability may be affected by these changes that are not considered by the previous models (X, Corey and viscous-coupling). The further study of flow structure effects on relative permeabilities will be presented in the next section.

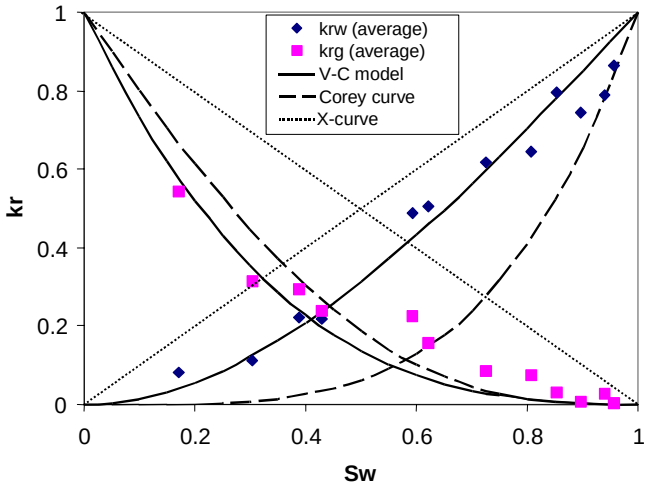

Figure 1.13: Comparison of average experimental relative permeability with the Corey-curve, X-curve and viscous-coupling models.

1.5 EFFECTS OF FLOW STRUCTURES ON RELATIVE PERMEABILITIES

Figure 1.10 shows that the channel flow is the dominant flow structure in our experiments. We might expect that these flows would be described by the X-model. Instead, they are rather in accordance with the viscous-coupling model. This can be explained by characterizing the morphology of phase channels and quantifying the magnitude of the "tortuosity" in this flow structure. A new approach will be discussed here to include the tortuosity created by the phases.

1.5.1 Tortuous-channel approach

Considering a simplified fracture space with a dimension of L (length) × W (width) × b (aperture) as shown in Figure 1.14, the fluids, water and gas, form ideal and straight channels through the fracture. From fundamentals of multiphase flow, the X-curve behavior is readily derived from Darcy's law and the cubic law by assuming negligible capillary pressure, gas slippage, inertia effect and wetting-phase stratified flow.

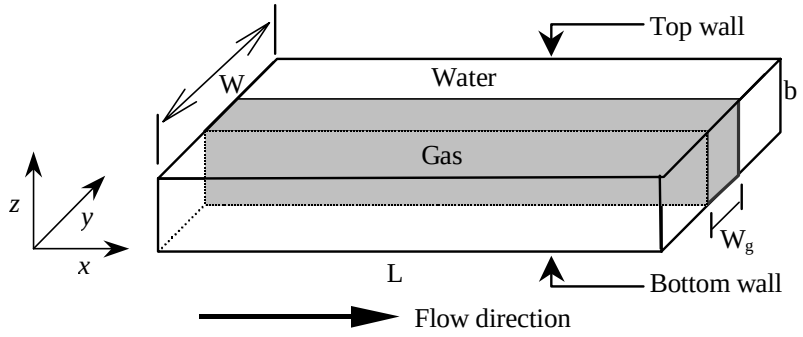

Figure 1.14: A simple model of a straight gas channel in a smooth-walled fracture.

Consequently, the straight phase-channel in the smooth-walled fracture will yield the X-curve relative permeability as shown by Romm (1966). However, as shown in this study, the actual flow structures in fractures seldom reach the ideal straight channel even though the fracture is smooth-walled. Most of the flow structures are either fingering or tortuous channels instead, and the relative permeability obtained from this experiment shows a deviation from X-curve as presented earlier in Figure 1.13. As a result, a physical, tortuous-channel approach to modify X-curve and take into account the channel tortuosity is required.

The concept of the tortuous-channel approach is based on the relationship between the fluid tortuosity and the relative permeability. As the channel flow observed in our study is tortuous (Fig. 9c), we define a tortuosity coefficient for the channel flow, τ_c, to characterizing its morphology. The definition of this apparent parameter is based on the area of the channel and the smallest bounding rectangle that covers the whole channel for a specific phase. As shown in Figure 1.15, the binary images processed from continuous true-color images were input into another image-processing program, which allows recognition and separation of the different flow structures. Then, the channel area, A_c (unit: pixel^2), length and width of the smallest bounding box, L_x and L_y (unit: pixel), were computed. The channel tortuosities for gas and water are then defined as:

$$\tau_{c,g} = \left(\frac{L_x L_y}{A_c}\right)_g \qquad \text{and} \qquad \tau_{c,w} = \left(\frac{L_x L_y}{A_c}\right)_w \tag{1.14}$$

As for the relative permeability, coefficient τ_c for each phase varies between 1 and ∞. This coefficient is related to the interfacial area and, consequently, allows quantifying the shear stress at the interface between the two fluids.

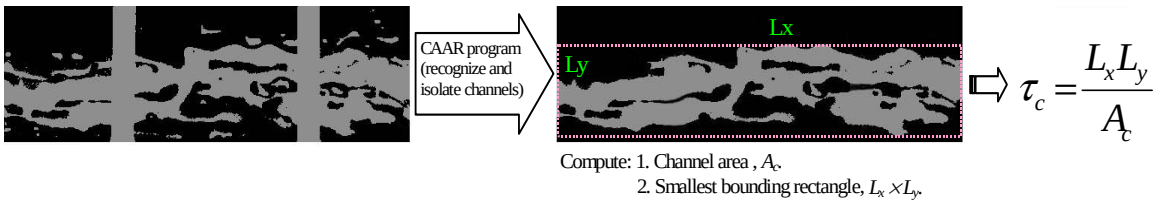

Figure 1.15: Evolution of channel tortuosity algorithm.

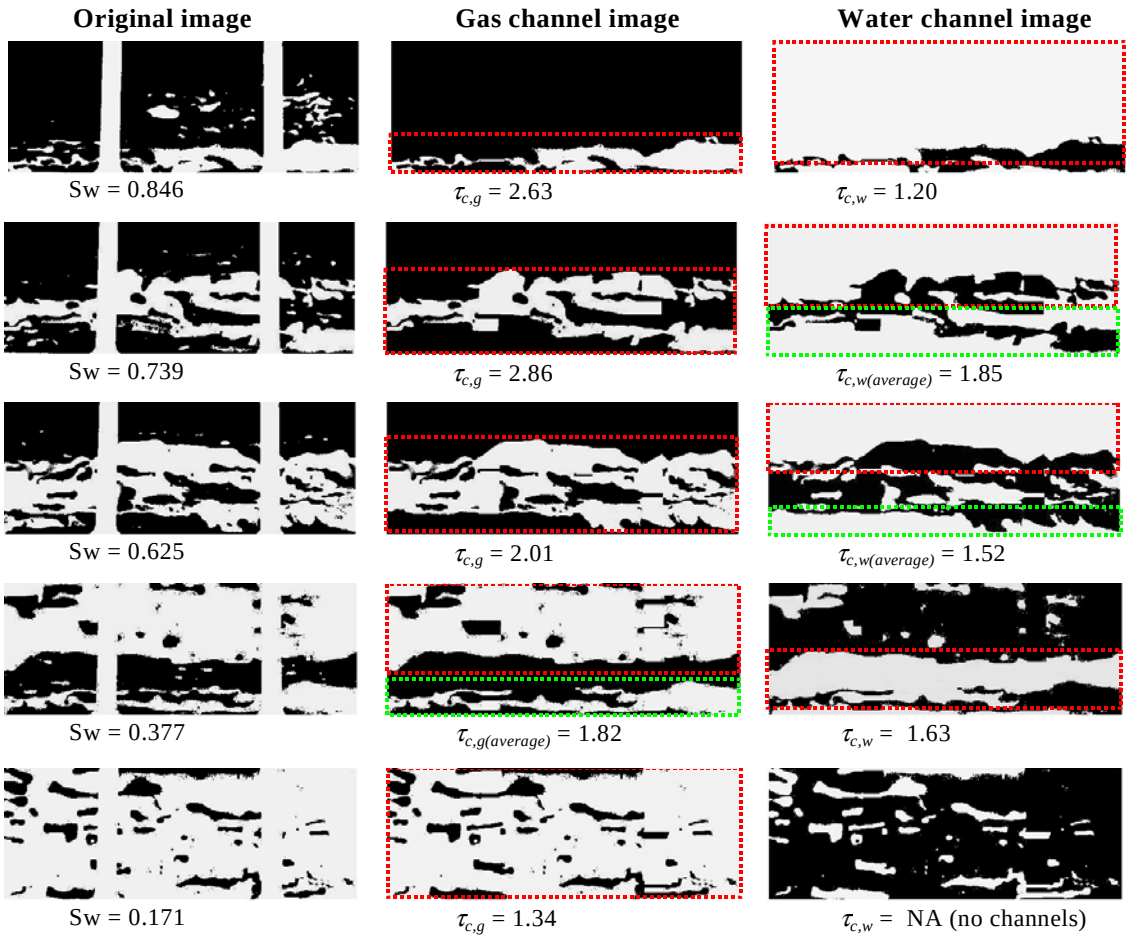

Figure 1.16: Representative images and corresponding processed gas-channel and water-channel images extracted from the CAAR image processing. (Phase channels are in white color in the channel images. Rectangles indicate the bounding boxes of the phase channels.)

In this study, thousands of continuous images extracted from the video of the experiment with a 0.33 second period were analyzed, and the tortuosities of gas and water were deduced for the channel flow configuration. Illustrations of these calculations are presented in Figure 1.16. It appears that water channels are less tortuous than gas channels. This may be due to the fact that the water-viscosity is higher than the gas-viscosity, and that water channels tend to adhere to longitudinal boundaries of the fracture, while gas channels flows in between.

In order to characterize the deviation from the X-model, we propose the following relationships:

$$k_{rw} = \frac{S_w}{\tau_{c,w}} \tag{1.15}$$

$$k_{rg} = \frac{S_g}{\tau_{c,g}} \tag{1.16}$$

This relationship assumes that the channel tortuosity is directly proportional to the deviation of X-curve behavior. In the case where each phase flows in the form of homogeneous strata (no dispersed phase), τ_{cw} = 1 and τ_{cg} = 1 and Equations 1.15 and 1.16 reduce to the X-model.

1.5.2 Reproduction of relative permeabilities

After deducing both water and gas tortuosities from the extracted images, the comprehensive water-phase and gas-phase relative permeabilities obtained from Equations 1.15 and 1.16 are shown in Figure 1.17. The original experimental results (Figure 1.12) are also provided in this figure. The results from the tortuous-channel approach show good reproduction of the experimental results in both water and gas phases. Thus, the tortuous-channel approach leads to low scatter in comparison with the experimental relative permeabilities. This is because some unstable phenomena, bubbles and slugs, were excluded and there are almost no sources of measurement errors in the tortuous-channel approach, except the image processing errors.

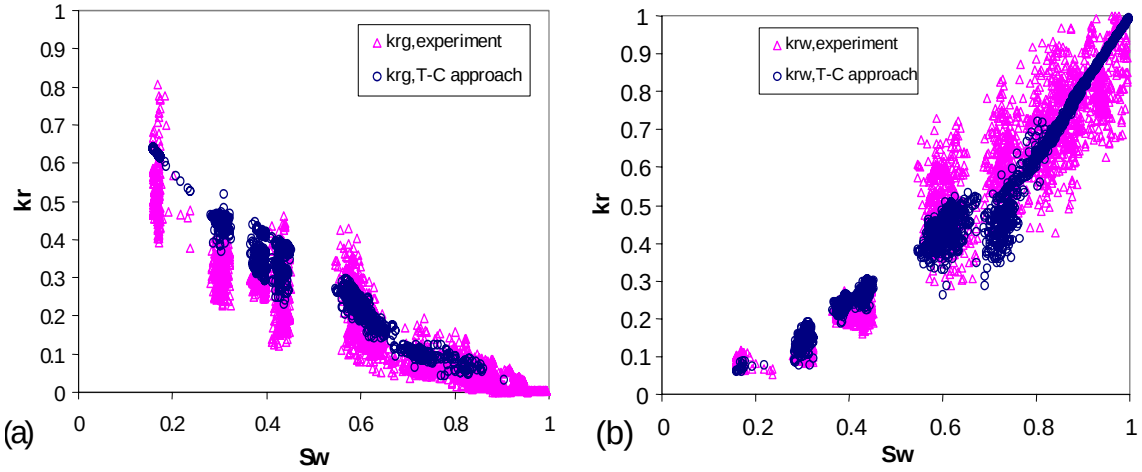

Figure 1.17: Relative permeabilities from tortuous-channel approach using phase tortuosities obtained from the processing of continuous images and its comparison with the original result: (a) gas phase, (b) water phase.

The mean tortuosity of gas and water channels was then computed by averaging all tortuosities in each run. Table 1.1 presents the mean channel tortuosity in each run for the experiments. The average phase tortuosity (reciprocal) versus the phase saturation is shown in Figure 1.18. Values of tortuosity reciprocal approach 1.0 when the channels increase straightness. A tortuosity value (or reciprocal) of 1.0 means perfect straight phase

channels. From these two plots, it is evident that the higher the phase saturation, the less tortuously those phase channels behave. The phase tortuosity values can be expressed by their phase saturations in second order approximations. The relative permeabilities calculated by using the average tortuosity in Table 1.1 and Equations 1.15 and 1.16 are presented in Figure 1.19. The values are in a good agreement with average experimental relative permeabilities for both gas and water phases. Aside from the generally matching performance, the tortuous-channel approach not only approximates the experimental result but closely reproduce some experimental points, especially the portion where the viscous-coupling model performs poorly.

Table 1.1: Averages of tortuous-channel parameter obtained from CAAR image processing program and the relative permeavility values for the tortuous-channel approach and experiment.

Saturation		Average channel tortuosities		Experiment results		Tortuous-channel approach	
S_w	S_g	$\tau_{c,g}$	$\tau_{c,w}$	$krg_{,expe}$	$krw_{,expe}$	$krg_{,T\text{-}C}$	$krw_{,T\text{-}C}$
0.957	0.043	NA*	1.038	0.002	0.863	NA	0.922
0.941	0.059	NA	1.065	0.028	0.788	NA	0.884
0.897	0.103	2.476	1.098	0.007	0.743	0.041	0.817
0.854	0.146	2.6	1.143	0.03	0.794	0.056	0.747
0.807	0.193	2.771	1.246	0.077	0.646	0.069	0.648
0.726	0.274	2.797	1.61	0.086	0.619	0.098	0.451
0.622	0.378	2.033	1.434	0.158	0.506	0.186	0.434
0.592	0.408	1.699	1.437	0.225	0.487	0.24	0.412
0.43	0.57	1.702	1.54	0.239	0.217	0.335	0.279
0.387	0.613	1.746	1.639	0.294	0.221	0.351	0.236
0.304	0.696	1.583	2.051	0.315	0.112	0.44	0.148
0.171	0.829	1.337	2.464	0.541	0.083	0.62	0.069

*: No channel detected.

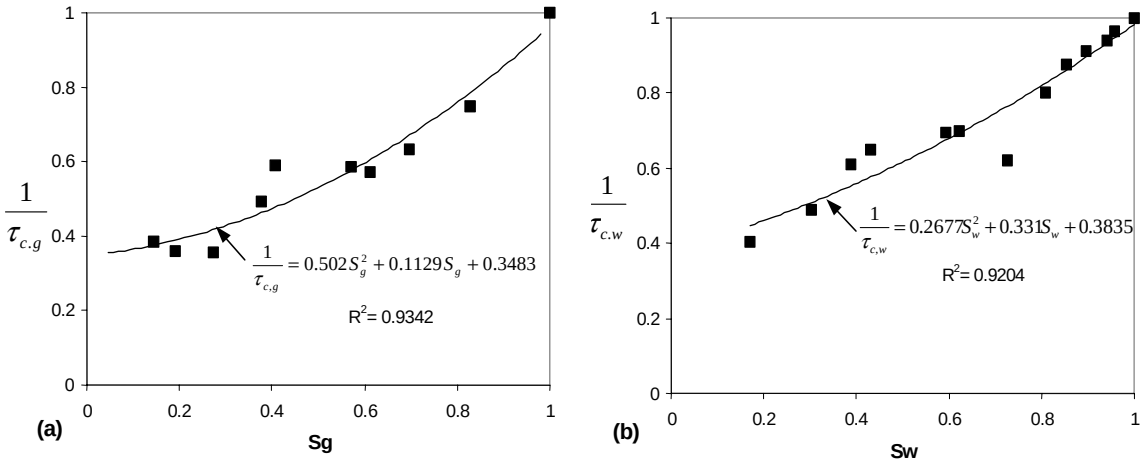

Figure 1.18: Reciprocal of average phase-channel tortuosity versus phase saturation in the air-water experiment: (a) gas phase, (b) water phase.

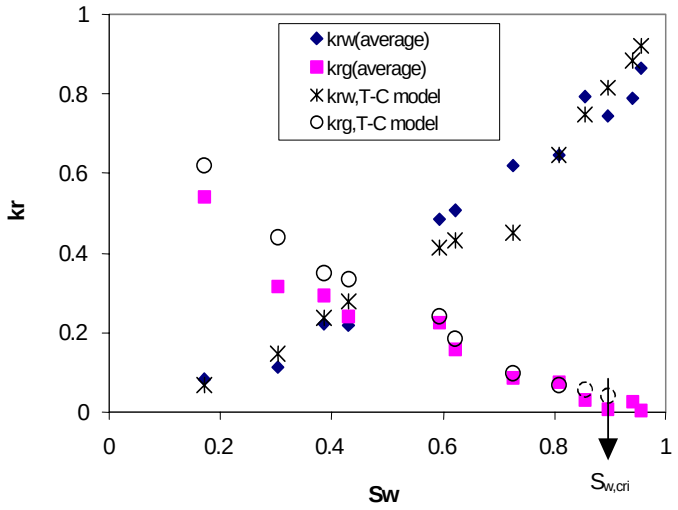

Figure 1.19: Comparison of average relative permeabilities from the tortuous-channel approach and from experiment. (The dash circles may contain more uncertainty due to few sampling points.)

1.5.3 Comparison with models

To compare the proposed tortuous-channel approach with other theoretical and empirical models mentioned previously, simple curve fits to express the tortuosity of phase channels mathematically were done in this preliminary stage. The optimal equations for fitting phase tortuosities as shown in Figure 1.18 are:

$$\frac{1}{\tau_{c,w}} = 0.2677S_w^2 + 0.331S_w + 0.3835 \tag{1.17}$$

$$\frac{1}{\tau_{c,g}} = 0.502S_g^2 + 0.1129S_g + 0.3483 \tag{1.18}$$

This leads Equations 1.15 and 1.16 to a tortuous-channel model:

$$k_{rw} = 0.2677S_w^3 + 0.331S_w^2 + 0.3835S_w \tag{1.19}$$

$$k_{rg} = 0.502S_g^3 + 0.1129S_g^2 + 0.3483S_g \tag{1.20}$$

The comparisons of the tortuous-channel model (Equations 1.19 and 1.20), viscous-coupling model and Corey-curve model with the experimental relative permeability are tabulated in Table 1.2. Figure 1.20 shows the comparison of two better models selected; the tortuous-channel model and viscous-coupling model. These two models perform equally accurate for the water phase. For the gas phase, the tortuous-channel model fits the experimental data better in high S_w range. On the other hand, the viscous-coupling model shows better performance in low S_w range. This model transition may indicate that the

dominant force shifts from the *xz*-plane shear stress to *xy*-plane shear stress, using the coordinate system as illustrated in Figure 1.14. Considering the gas phase, except in low S_w range, most of the force contributed by the flow is applied to exploring and sustaining the gas region horizontally (in the *xy* plane). Therefore, the magnitude of the *xy*-plane shear stress was relatively small and negligible. This leads to the suitability of the tortuous-channel approach. However, when most of the fracture space was occupied by the gas at low S_w, less force was used to sustain the gas region horizontally (*xy* plane) since the gas channels were wider and straighter. Instead, most of the force was contributed by the *xy*-plane shear force because of the importance of the vertical (*x*-*z*) stratified flow at this stage. This will be close to the viscous-coupling behavior.

Table 1.2: Comparison of experimental and modeling results for the air-water relative permeability.

Saturation		Experiment Results		Tortuous-channel model*		Viscous-coupling model		Corey curve†		X-curve	
S_w	S_g	$krg,_{expe}$	$krw,_{expe}$	$krg,_{T\text{-}C}$	$krw,_{T\text{-}C}$	$krg,_{V\text{-}C}$	$krw,_{V\text{-}C}$	$krg,_{Corey}$	$krw,_{Corey}$	$krg,_{X}$	$krw,_{X}$
0.957	0.043	0.002	0.863	0.015	0.905	0.001	0.935	3E-06	0.914	0.043	0.957
0.941	0.059	0.028	0.788	0.021	0.877	0.002	0.911	1E-05	0.882	0.059	0.941
0.897	0.103	0.007	0.743	0.038	0.804	0.004	0.846	1E-04	0.797	0.103	0.897
0.854	0.146	0.030	0.794	0.055	0.736	0.007	0.783	5E-04	0.714	0.146	0.854
0.807	0.193	0.077	0.646	0.075	0.666	0.013	0.715	0.001	0.628	0.193	0.807
0.726	0.274	0.086	0.619	0.114	0.556	0.028	0.600	0.006	0.488	0.274	0.726
0.622	0.378	0.158	0.506	0.175	0.431	0.064	0.460	0.02	0.332	0.378	0.622
0.592	0.408	0.225	0.487	0.195	0.399	0.078	0.422	0.028	0.292	0.408	0.592
0.430	0.570	0.239	0.217	0.328	0.247	0.196	0.238	0.105	0.125	0.570	0.430
0.387	0.613	0.294	0.221	0.371	0.214	0.241	0.196	0.141	0.094	0.613	0.387
0.304	0.696	0.315	0.112	0.466	0.155	0.348	0.125	0.235	0.048	0.696	0.304
0.171	0.829	0.541	0.083	0.652	0.077	0.577	0.041	0.472	0.009	0.829	0.171

*: using Equations 1.19 and 1.20.

†: by setting $S_{rw} = S_{rg} = 0$.

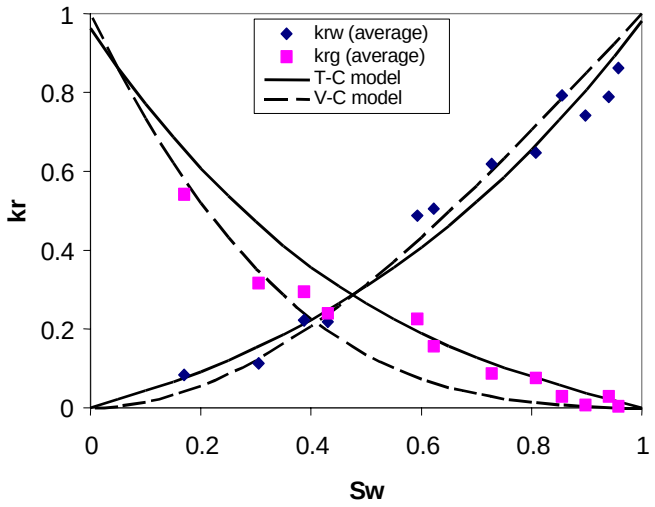

Figure 1.20: Comparison of the experimental relative permeability with the tortuous-channel model and viscous-coupling model for the air-water experiment.

To compare these models visually and quantitatively, the comparison between measured and predicative water saturation and relative permeabilities was made using Equations 1.5 to 1.11 and Equations 1.19 and 1.20. The result is shown in Figure 1.21. The statistical analysis of the absolute errors and standard deviations between experimental and modeling relative permeabilities and saturations is also presented in Table 1.3. Apparently, both the viscous-coupling model and tortuous-channel model can interpret and predict the relative permeability and water saturation with good accuracy, whereas both the X-curve and Corey-curve models show worse performance. From the statistical mean absolute error and standard deviation, the tortuous-channel model performs slightly better than the viscous-coupling model in predicting both relative permeability and water saturation. To sum up, from validations of both the comprehensive and average results and model comparisons, the proposed tortuous-channel approach can interpret the relative permeabilities at the air-water experiment successfully. This tells us that the relative permeability is dependent on flow structure. At the moment, the flow structure prediction is a complicated and immature subject.

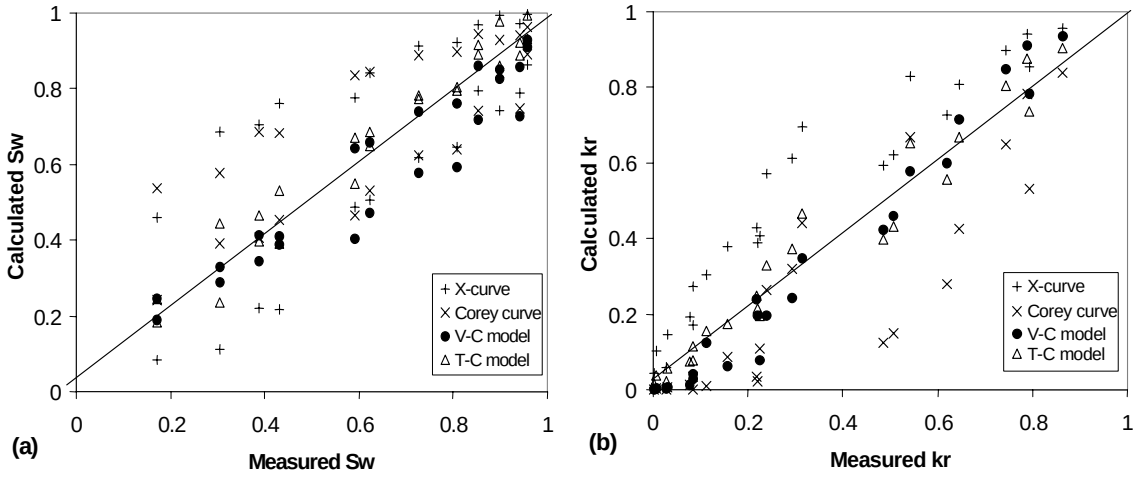

Figure 1.21: Comparison between measured and calculated (a) water saturation, (b) relative permeability.

Table 1.3: Statistical analysis descriptors (mean absolute error and standard deviation) of relative permeabilities and water saturation between experiment and models.

Models	k_r		S_w	
	$MAE^{\dagger}(k_r)$	$\sigma^{\ddagger}$	$MAE(S_w)$	σ
X-curve	0.1633	0.0920	0.1633	0.0920
Corey curve (Corey, 1954)	0.1207	0.1147	0.1313	0.1008
Viscous-coupling model*	0.0496	0.0377	0.0729	0.0653
Tortuous-channel model (this work)	0.0485	0.0384	0.0505	0.0325

* : Fourar and Lenormand, (1998)

† : Mean absolute error; $MAE(Y) = \frac{1}{N}\sum_1^N \left|Y_{\text{expe},i} - Y_{\text{model},i}\right|$

‡ : standard deviation, $\sigma = \sqrt{\frac{1}{N-1}\sum_1^N \left(\left|Y_{\text{expe},i} - Y_{\text{model},i}\right| - MAE(Y)\right)^2}$

1.6 CONCLUSION

Experimental results of air-water flow through a smooth-walled fracture were presented. Using a high-speed data acquisition system and digital image processing technology, the experimental apparatus was able to characterize the unstable nature of the flow.

Different flow configurations were visualized: bubbles, slugs and channels. Experimental results of pressure drop, flow rates, and saturation were interpreted by using the relative permeability concept and compared to three models from the literature: the X-model, the Corey-model and the viscous-coupling model. The results were well described by the viscous-coupling model showing more interactions between phases than the X-model, but less interference than predicted by the Corey-model.

By introducing the tortuous-channel concept, we showed that the deviation from the X-model is due to the flow configuration. The proposed tortuous-channel approach has reproduced both original and average experimental relative permeabilities. After applying mathematical expressions of phase tortuosity coefficients, the preliminary tortuous-channel model performed best among other models. Therefore the concept of the tortuosity coefficient may allow modeling two-phase flow in a fracture whatever the flow configuration. To this end, the coefficient τ_c must be related physically to the shear stress at the surface between the two fluids and to the interface area. Unfortunately, up to now there is no model that allows us to predict flow structures in a fracture. It was also noticed that the values of the gas-phase relative permeability from the experiment tend to shift from the proposed tortuous-channel model to the viscous-coupling model in the low water saturation range, which may be because the vertical stratified flow is no longer negligible in this situation.

2. CHARACTERIZATION OF CAPILLARY PRESSURE IN GEOTHERMAL ROCKS USING FRACTAL METHODS

This research project is being conducted by Senior Research Engineer Kewen Li and Prof. Roland Horne. The objective of this project is to determine capillary pressures in heterogeneous geothermal rocks. It was found that we can calculate fractal dimension of a porous medium using three different methods and use the approach to estimate capillary pressure in real rocks.

2.1 SUMMARY

There have been three main models applied to infer fractal dimensions of reservoir rock from capillary pressure curves. In this study, the three fractal models were derived theoretically and found to be interrelated. Capillary pressure curves of different rock samples were measured using a mercury intrusion technique. The values of fractal dimension were calculated using the three fractal models and the results were compared. The values of fractal dimension calculated from two models were almost the same and ranged from 2 to 3. However the fractal dimensions calculated using the other model were different and ranged from 1 to 2. It was found that the Brooks-Corey capillary pressure model did not work for any of the geothermal core samples studied (only for sandstone cores) but the fractal models work satisfactorily in all cases. The fractal approach was verified using frequency graphs of the pore size distribution of the rock samples.

2.2 INTRODUCTION

Heterogeneity of the reservoir rock is a key parameter in geothermal reservoir engineering; it controls production performance, injectability, and ultimate energy recovery, etc. It would be helpful for engineers to have an appropriate approach to characterize the heterogeneity of reservoir rock quantitatively. However this has been a challenge for a long time.

There have been many methods to characterize heterogeneity of objects in nature. Among the approaches, fractal geometry has been utilized in many areas, including the characterization of rock heterogeneity in reservoirs. Many researchers have studied the fractal nature of reservoir rocks and other porous media in the past two decades.

Katz and Thompson1 (1985) showed that the pore spaces of several sandstones are fractal by using scanning electron microscopy (SEM) and optical data. Katz and Thompson (1985) developed a method to predict rock porosity using the fractal statistics.

Wong et al. (1986) studied the microstructure of sedimentary rocks by using small-angle neutron scattering (SANS) and found that the pore spaces of sandstones and shales show fractal nature because of the presence of clay.

Friesen and Mikula (1987) proposed a technique to infer fractal dimension of coal particles from capillary pressure data by mercury intrusion porosimetry. Later Pérez Bernal and

Bello López (2000) calculated the fractal dimensions of building stones using this approach.

Hansen and Skjeltorp (1988) conducted direct measurements of the fractal volume and surface dimensions of sandstones; they evaluated fractal dimensions using box-counting techniques. Hansen and Skjeltorp (1988) demonstrated the dependence of rock permeability on the values of fractal dimension.

Krohn (1988) measured the fractal properties of sandstones, shales, and carbonates using a statistical analysis of structural features on fracture surfaces. Krohn (1988) found that the values of porosity calculated using the fractal model were less than or equal to the measured values. The remaining porosity might be associated with Euclidean pores. This may explain the difference between the measured porosity and the porosity estimated by the fractal model proposed by Katz and Thompson (1985).

Lenormand (1990) investigated gravity drainage in micromodels and proposed that the production rate may be a power-law function of production time. The exponent of this function was associated with the fractal nature of the micromodels. Lenormand (1990) also reported a relative permeability model derived from fractal modeling of porous media.

Angulo and Gonzalez (1992) reported another approach to evaluate fractal dimensions using capillary pressure data from mercury intrusion tests. The idea was to plot the volume of mercury intruded into rock versus capillary pressure; the relationship between the two parameters was supposed to be a power-law function. Angulo and Gonzalez (1992) related the scaling exponent to the pore bulk fractal dimensions.

Shen and Li (1994 and 1995) and Li and Horne (2003), also developed a method to calculate fractal dimension and characterize the heterogeneity of rock using capillary pressure data from mercury intrusion tests. The number of pores was estimated from the capillary pressure curves first and then the radius of pore throat was inferred. The number of pores was plotted versus the radius of pore throat. The relationship between the number of pores and the radius of pore throat was seen to be a power-law function.

According to the fractal curves inferred from capillary pressures measured by mercury intrusion, Shen and Li (1994) found that the part of porous media with large pores was not fractal (domain I) but the remaining part with small pores was fractal (domain II or domain III). This is consistent with the results of porosity measurements by Krohn (1988) who reported that the measured values of porosity were greater than or equal to the values calculated using fractal model proposed by Katz and Thompson (1985). The reason may be that the part with large pores was not considered in the fractal porosity model.

Shen and Li (1994 and 1995) observed two domains (domain II and domain III) with different fractal dimensions in the fractal part of some porous systems. Shen and Li (1995) also reported the experimental relationship between the recovery and the fractal dimension

of domain II as well as the relationship between the initial water saturation and the fractal dimension of domain III with smaller pores.

Li and Horne (2003) found that the capillary pressure curves measured by mercury intrusion in The Geysers graywacke rock could not be represented using the frequently-used Brooks-Corey (1964) model but could be modeled using a fractal approach.

Attention has also been paid to the application of fractal modeling of porous media in reservoir engineering. Moulu et al. (1997) developed a three-phase relative permeability model based on the fractal representation of rock. Toledo et al. (1994) proposed fractal models for capillary pressure, water relative permeability, electrical conductivity, and capillary dispersion. Few experimental data were used to test the models. Abdassah (1996) derived an electrical resistivity model according to the fractal modeling of thin-sections.

Summarizing the literature in this area, there have been many methods to infer the fractal dimension of rock. These methods include SEM, SANS, thin-section, and mercury intrusion. Only the mercury intrusion technique was considered in this study. There have been three main models to infer fractal dimensions from capillary pressure curves measured by mercury intrusion. Few studies have investigated the relationship between these models. On the other hand, results obtained from different fractal techniques may be inconsistent.

In this study, capillary pressure curves of different rocks were measured using mercury intrusion. It was proven that three approaches used to calculate fractal dimension from capillary pressure curves could be derived from each other. Fractal dimensions were calculated with the three fractal models and the results were compared. The fractal approach used to characterize the rock heterogeneity was verified qualitatively using the frequency graphs of pore size distribution inferred from capillary pressure curves. Also studied was the comparison of fractal dimension inferred from intrusion capillary pressures with that inferred from extrusion capillary pressures in the same core sample.

2.3 THEORY

As mentioned previously, there have been three main models to calculate fractal dimension from capillary pressure curves. The three fractal models proposed by different researchers are derived theoretically in this section.

An important feature of a fractal object in nature is the self-affinity with a dimension that is fractal rather than integer. This feature can be represented mathematically by a power-law function:

$$N(r) \propto r^{-D_f} \tag{2.1}$$

where r is the radius (or characteristic length) of a unit chosen to fill the fractal object, $N(r)$ is the number of the units (with a radius of r) required to fill the entire fractal object, and

D_f is the so-called fractal dimension. The fractal dimension is a representation of the heterogeneity of the fractal object. The greater the fractal dimension, the more heterogeneous the fractal object.

Capillary pressure curves measured by a mercury intrusion technique are often used to infer the pore size distribution of rock samples. In making this inference, rock with solid skeleton and pores is represented by using a capillary tube model. $N(r)$ can be calculated easily once capillary pressure curves are available. The unit chosen in this study was a cylindrical capillary tube with a radius of r and a length of l. So the volume of the unit is equal to $\pi r^2 l$ and $N(r)$ at a given radius of r is then calculated easily.

Once $N(r)$ is known, the value of fractal dimension, D_f, can be determined from the relationship between $N(r)$ and r. The relationship between $N(r)$ and r should be linear on a log-log plot if the pore system of the rock is fractal.

According to the capillary tube model and the previous description, $N(r)$ can be expressed as follows:

$$N(r) = \frac{V_{Hg}}{\pi r^2 l} \tag{2.2}$$

where l is the length of a capillary tube and V_{Hg} is the cumulative volume of mercury intruded into the rock sample when capillary pressure is measured.

Combining Eq. 2.1 and Eq. 2.2:

$$\frac{V_{Hg}}{\pi r^2 l} \propto r^{-D_f} \tag{2.3}$$

Arranging Eq. 2.3:

$$V_{Hg} \propto r^{2-D_f} \tag{2.4}$$

Considering a capillary tube model, the capillary pressure can be expressed as follows:

$$P_c = \frac{2\sigma \cos\theta}{r} \tag{2.5}$$

where P_c is the capillary pressure, σ is the surface tension, and θ is the contact angle.

Substituting Eq. 2.5 into Eq. 2.4:

$$V_{Hg} \propto P_c^{-(2-D_f)} \tag{2.6}$$

The mercury saturation is calculated as follows:

$$S_{Hg} = \frac{V_{Hg}}{V_p} \tag{2.7}$$

where S_{Hg} is the mercury saturation and V_p is the pore volume of the core sample.

Substituting Eq. 2.7 into Eq. 2.6:

$$S_{Hg} = aP_c^{-(2-D_f)} \tag{2.8}$$

where a is a constant.

According to Eq. 2.8, the saturation of mercury intruded into the rock is a power-law function of capillary pressure and the fractal dimension can be obtained by drawing the mercury saturation versus capillary pressure on a log-log plot. This method is similar to the technique used by Angulo and Gonzalez (1992).

Differentiating Eq. 2.8:

$$\frac{dS_{Hg}}{dP_c} \propto P_c^{-(3-D_f)} \tag{2.9}$$

Eq. 2.9 is similar to the equation derived by Friesen and Mikula (1987):

$$\frac{dS_{Hg}}{dP_c} \propto P_c^{-(4-D_f)} \tag{2.10}$$

Note that we would obtain the same equation if a three-dimensional pore model, instead of a two-dimensional capillary tube model, were used to calculate the number of pores in porous media. Fractal dimension can also be calculated from capillary pressure data according to Eq. 2.9.

One can see that the approach (Eq. 2.8) used by Angulo and Gonzalez (1992) can be derived from Eq. 2.1; and the model (Eq. 2.9 or 2.10) proposed by Friesen and Mikula (1987) can be derived from Eq. 2.8. This demonstrates that the three fractal models (Eqs. 2.1, 2.8, and 2.9) can be derived from each other. Theoretically the values of fractal dimension calculated using the three approaches should be the same. However the results were actually different. This will be demonstrated in the next section and discussed in more detail.

2.4 EXPERIMENTAL MEASUREMENTS

Mercury intrusion tests were conducted in three reservoir core samples and one Berea sandstone core sample. The reason for the selection of mercury intrusion tests to measure capillary pressure curves is that the surface tension of mercury and the contact angle are

well known and constant during an experiment. With this feature, the measured capillary pressure curves should be a good representation for the pore structure of rock.

The measured porosities of the three reservoir core samples were 24.09% (core S1), 26.32% (core S2), and 27.11% (core S3); the air permeabilities were 206, 935, and 2131 md respectively. The porosity of the Berea sandstone sample was about 23.0% and the air permeability was about 804 md.

The surface tension of air/mercury is 480 mN/m and the contact angle through the mercury phase is 140^{o} according to the results reported by Purcell (1947).

2.5 RESULTS

The values of fractal dimension were calculated from experimental data of capillary pressure using the three approaches represented by Eqs. 2.1, 2.8, and 2.9 respectively. The results are presented and analyzed in this section.

Fig. 2.1 shows the experimental data of capillary pressure curves of the three reservoir core samples. In Fig. 2.1, capillary pressure was plotted against wetting-phase saturation (the wetting-phase was air in this study). Qualitatively one can see from Fig. 2.1 that the heterogeneity of the three core samples was significantly different according to the curvatures of the capillary pressure curves. Core S1 was the most heterogeneous and core S3 was the most homogeneous. It is expected that the values of fractal dimension of the three core samples have the following relationship: D_f(S1)>D_f(S2)>D_f(S3).

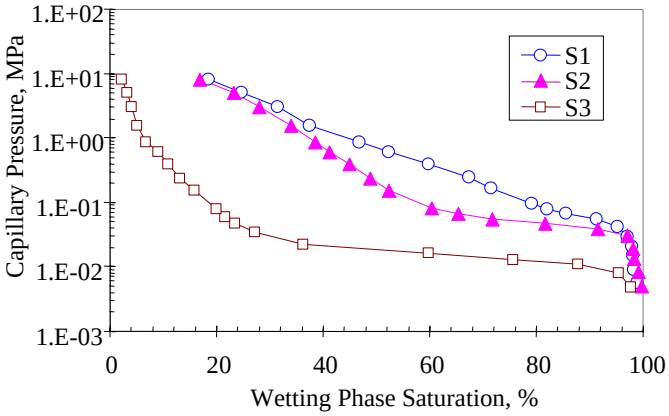

Figure 2.1: Capillary pressure curves of the three reservoir core samples.

As mentioned previously, there are three main approaches (Eqs. 2.1, 2.8, and 2.9) to infer fractal dimension from capillary pressure curves. To test whether the values of fractal dimension calculated using the three approaches are the same, the capillary pressure curves were transferred and plotted in Figs. 2.2, 2.3, and 2.4 according to Eqs. 2.1, 2.8, and 2.9. One can see in Fig. 2.2 that all the curves of $N(r)$ vs. r are linear on a log-log plot, which implies that the pore systems of the three core samples are fractal and can be characterized using the theories of fractal geometry. Note that some data points with large pore throat diameters in Fig. 2.2 are off the straight lines. This implies that the pore system consisting

of large pore throats may not be fractal, which is consistent with the observations of other researchers (Krohn, 1988, Shen and Li, 1994). The values of fractal dimension were calculated using Eq. 2.1 (Method I) and the results are listed in Table 2.1. The results show that the values of fractal dimension of the three core samples range from 2.06 to 2.45 and have the relationship: D_f(S1)>D_f(S2)>D_f(S3), as expected. The values of fractal dimension represent the extent of heterogeneity. The core with greater fractal dimension has greater heterogeneity.

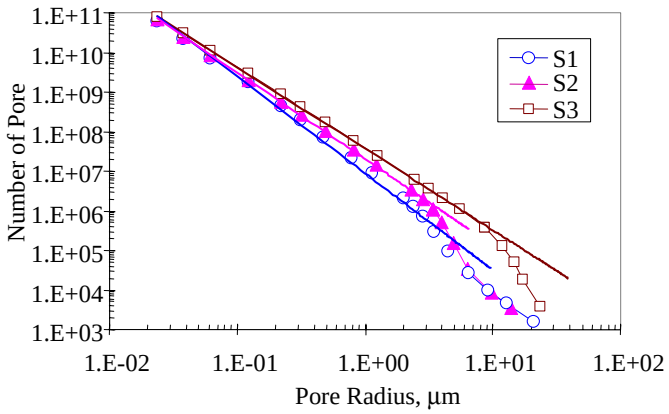

Figure 2.2: Relationships between N(r) *and* r *of the three reservoir core samples.*

Fig. 2.3 shows the relationship between mercury saturation and capillary pressure. As foreseen from Eq. 2.8, the three curves are all linear when the capillary pressure is greater than a specific value. Fractal dimensions were calculated based on the linear part shown in Fig. 2.3 using Eq. 2.8 (Method II) and the results are listed in Table 2.1. One can see that the values of fractal dimensions calculated using Method I and Method II are almost the same for the three reservoir core samples. Fig. 2.3 also demonstrates that the pore system with large pores may not be fractal.

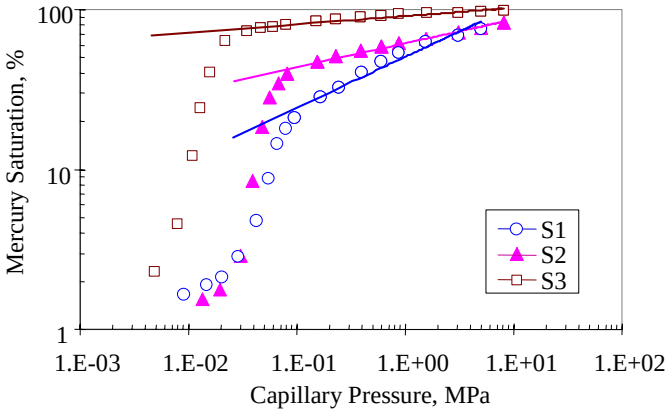

Figure 2.3: Relationships between mercury saturation and capillary pressure of three core samples.

Fig. 2.4 plots the fractal curves transferred from the capillary pressure data shown in Fig. 2.1 according to Eq. 2.9 (Method III). The data points in Fig. 2.4 are more scattered than the data in Figs. 2.2 and 2.3. The values of fractal dimensions calculated using Method III are also listed in Table 2.1. Although the results show that D_f(S1)>D_f(S2)> D_f(S3), the values of fractal dimensions are significantly different from those calculated using Method I and Method II. The fractal dimensions calculated using Method III was in the range from 1 to 2 rather than from 2 to 3.

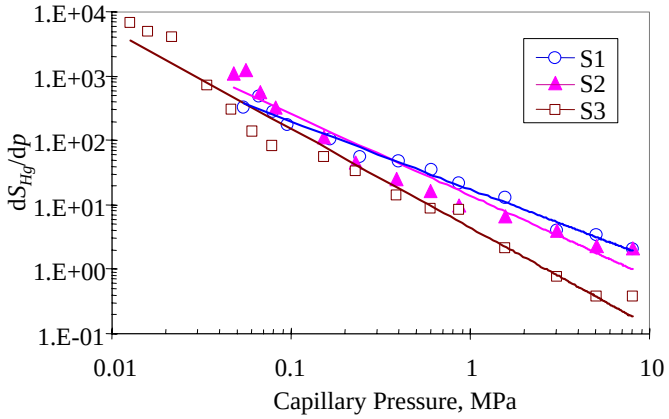

Figure 2.4: Relationships between dS_{Hg}/dP_c and P_c of three core samples.

Table 2.1: Fractal dimensions calculated using three models.

Sample		S1	S2	S3	Berea
ϕ (%)		24.09	26.32	27.11	23.0
k (md)		206	935	2131	804
D_f	Method I	2.45	2.18	2.06	2.05
	Method II	2.32	2.15	2.05	2.05
	Method III	1.94	1.73	1.47	1.45

Another approach used frequently to represent capillary pressure curves is the Brooks-Corey model (1964). This approach plots capillary pressure versus normalized wetting-phase saturation in logarithmal coordinations. The capillary pressure curves shown in Fig. 2.1 were transferred in such a way and the results are shown in Fig. 2.5. The normalized wetting-phase saturation is calculated as follows:

$$S_w^* = \frac{S_w - S_{wr}}{1 - S_{wr}} \tag{2.11}$$

where S_w^* is the normalized wetting-phase saturation, S_w is the wetting-phase saturation, and S_{wr} is the residual saturation of the wetting-phase.

One can see from Fig. 2.5 that the capillary pressure curve of core S3 is linear on a log-log plot, which implies that the capillary pressure curve can be represented using the Brooks-Corey model (1964). However the capillary pressure curves of the other two rock samples are nonlinear, which implies that the capillary pressure curves may not be represented using the Brooks-Corey model. Note that all the three fractal curves shown in Fig. 2.2 are linear.

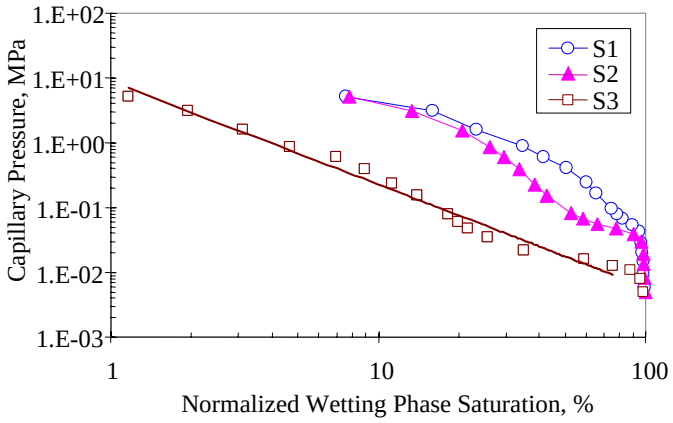

Figure 2.5: Representation of the capillary pressure curves of three core samples using Brooks-Corey model.

According to the values of fractal dimensions calculated using the three fractal models (Eqs. 2.1, 2.8, and 2.9), core S1 has the greatest heterogeneity and core S3 has the greatest homogeneity. To provide further evidence of the heterogeneity of the three core samples, the pore size (pore throat radius) distributions inferred from capillary pressure measurements are shown in Figs. 2.6-2.8. Rock heterogeneity can be observed qualitatively from the frequency graph of pore size distribution. One can see from Fig. 2.6 that the pore size distribution of core S1 is wide and has multiple peaks. Fig. 2.8 shows that the pore size distribution of core S3 is narrow and has only one peak. This implies that core S1 is more heterogeneous than core S3, as indicated by the values of fractal dimensions listed in Table 2.1.

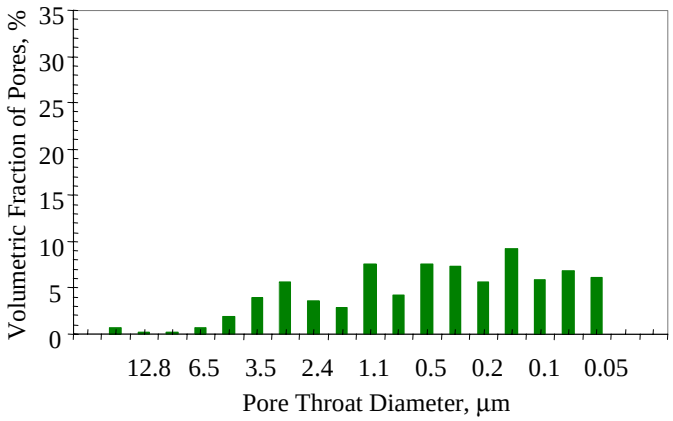

Figure 2.6: Pore size distribution of core S1.

Both intrusion and extrusion capillary pressure curves of Berea sandstone were measured and the results are plotted in Fig. 2.9. The fractal curves transferred using Method I are shown in Fig. 2.10. The fractal dimensions in the intrusion and the extrusion cases calculated using Method I are the same and the value is listed in Table 2.1. Figs. 2.11 and 2.12 show the fractal curves transferred using Method II and Method III. One can see that the fractal dimensions in the intrusion and the extrusion cases calculated using Method II and Method III are also almost the same. Note that the fractal dimension of Berea sandstone listed in Table 2.1 is the value in the intrusion case.

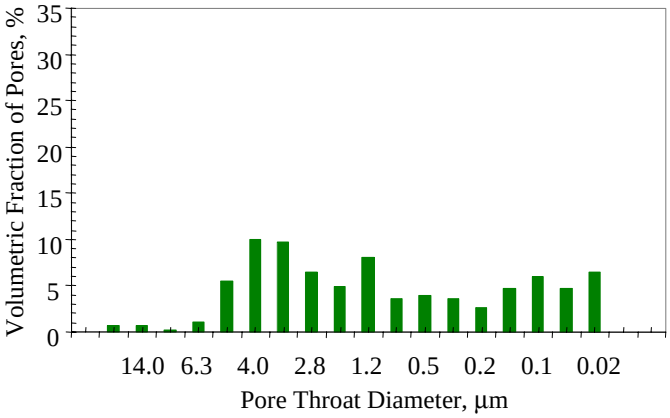

Figure 2.7: Pore size distribution of core S2.

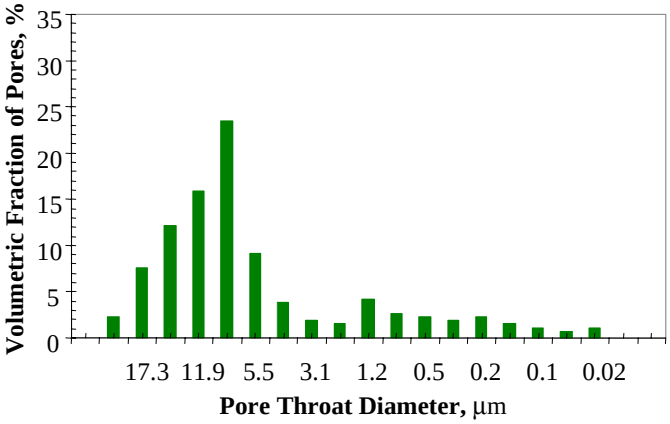

Figure 2.8: Pore size distribution of core S3.

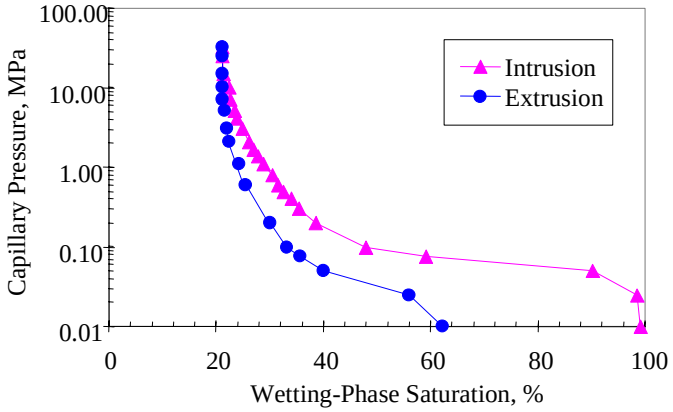

Figure 2.9: Capillary pressure curves of Berea sandstone (intrusion and extrusion).

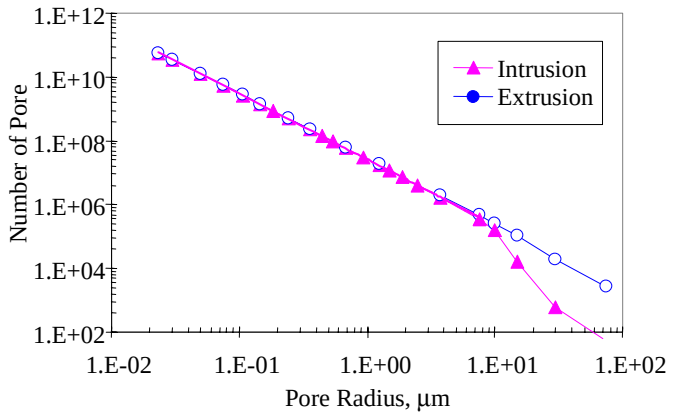

Figure 2.10: Fractal curves of Berea sandstone in the intrusion and the extrusion cases (Method I).

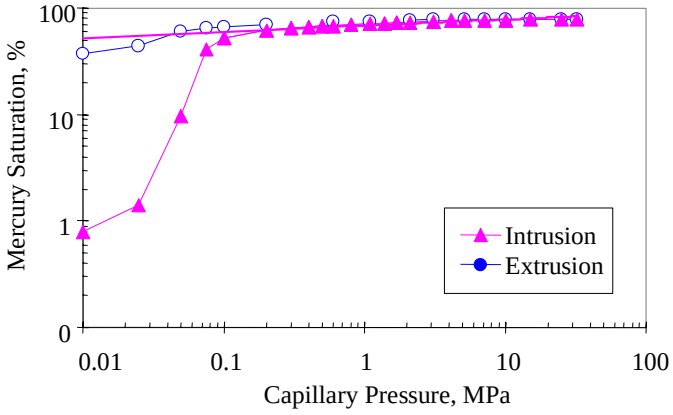

Figure 2.11: Fractal curves of Berea sandstone in the intrusion and the extrusion cases (Method II).

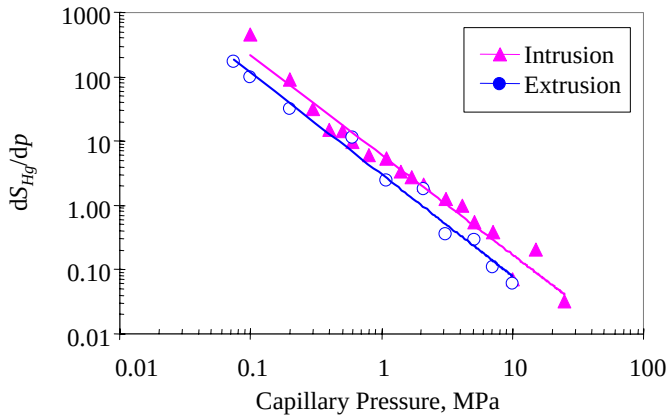

Figure 2.12: Fractal curves of Berea sandstone in the intrusion and the extrusion cases (Method III).

The results discussed in this section demonstrated that the fractal dimension characterizes the heterogeneity of rock satisfactorily.

2.6 DISCUSSIONS

According to the studies in this work, it has been found that almost equal fractal dimensions could be obtained using Method I and Method II. However the fractal dimensions inferred using Method III are substantially different and are unexpectedly less than 2. The data points are very scattered if Method III is used. The reason is not clear. Probably, the error is enlarged after differentiating the mercury saturation and the capillary pressure. Nonetheless it may be too early to declare Method III to be invalid.

The significance of calculating fractal dimensions of rock and characterizing heterogeneity is the application in developing relative permeability models, capillary pressure models, and predicting production rate, *etc*.

It is known that many reservoir properties such as production performance, and ultimate energy recovery depend on the heterogeneity of rock. It is helpful to correlate these parameters if the heterogeneity of rock can be represented quantitatively and properly. There are not many parameters available to do so. The results in this study show that fractal dimension inferred from capillary pressure curves measured by mercury intrusion, either calculated using Method I or Method II, can characterize the heterogeneity of rock quantitatively and properly. As described previously, there are many areas where the concept of fractal dimension and the theories of fractal geometry can be applied.

2.7 CONCLUSIONS

Based on the present study, the following conclusions may be drawn:

1. Fractal dimension estimated from capillary pressure curves measured by mercury intrusion can be used to characterize the heterogeneity of rock samples quantitatively.
2. Three approaches used by earlier authors to infer fractal dimension from capillary pressure curves can be derived theoretically from each other.

3. The values of fractal dimension calculated using three approaches may be different but the relationship with heterogeneity of rock is similar, that is, the greater the fractal dimension, the greater the heterogeneity of the rock.
4. The fractal dimension inferred from the intrusion capillary pressure curve is almost the same as that from the extrusion capillary pressure curve in Berea sandstone.
5. The capillary pressure curves of two core samples among three are not linear but the fractal curves of all the three core samples are linear in a log-log plot.

3. FRACTURED ROCK RELATIVE PERMEABILITY

This project is being conducted by Research Assistant Anson L. Villaluz, Research Associate Kewen Li and Prof. Roland N. Horne. The objective is to obtain measurements of steam-water relative permeability in real fractured rocks from geothermal reservoir. This work is an extension of our earlier steam-water relative permeability studies which have mostly considered artificially uniform and high permeability rocks. Now that the relative permeability mechanisms have been understood, we are ready to embark on the more difficult measurements using heterogeneous, low permeability rocks from geothermal reservoirs.

3.1 BACKGROUND

Steam-water relative permeability and capillary pressure are important data for geothermal reservoir engineering. The Stanford Geothermal Program (SGP) has succeeded in making fundamental measurements of steam-water flow in porous media and made significant contribution to the industry. One of the important problems left to undertake is the measurement of steam-water relative permeability and capillary pressure in geothermal rock (most of the previous study was conducted in high permeability sandstone as a well-controlled test material.).

Using our existing steady-state CT method, we have measured steam-water relative permeability and capillary pressure in rock with permeability above 1 md (10^{-13} cm^2). We can obtain the in-situ fluid saturation simultaneously. For the geothermal rock with permeability smaller than 1 md (10^{-13} cm^2), the steady-state CT method would work but it would take an extremely long time to conduct the experiments (weeks or even months). Hence the CT method is not practical to measure steam-water relative permeability in geothermal rocks.

To overcome this difficulty, we have embarked on different approach, by measuring the relative permeability curves in separate sections. We have concluded from our experimental data (Satik, 1998; Horne *et al*., 2000; Mahiya, 1999; O'Connor, 2001; Li and Horne, 2000a) that steam-water relative permeability follows the Corey model and steam-water capillary pressure follow the Brooks-Corey model. We can measure the end-point steam-water relative permeability and saturation in the geothermal rock with permeability smaller than 1 md using our existing steady-state CT method or the direct weighing method developed by Li *et al*. (2001). Then the whole curve of steam-water relative permeability can be obtained using the Corey model and the capillary pressure curve can be obtained using the Brooks-Corey model. We plan to confirm the applicability of this approach first with nitrogen-water experiments, which are very much easier to conduct then the steam-water flows. This work was begun by Habana (2002), but ran into experimental difficulties.

The experimental study performed by Habana (2002) on a real fractured geothermal core showed results with pressure spikes occurring periodically during single-phase water injection. Erratic pressure spikes were observed during nitrogen-water relative permeability experiment in the same study. Some of the results are presented in Figures

3.1 and 3.2. The appearance of these transient effects indicated a difficulty with the experimental configuration, and prevented the measurement of relative permeability. In the continuation of this study, the apparatus will be redesigned and reconstructed to overcome these problems.

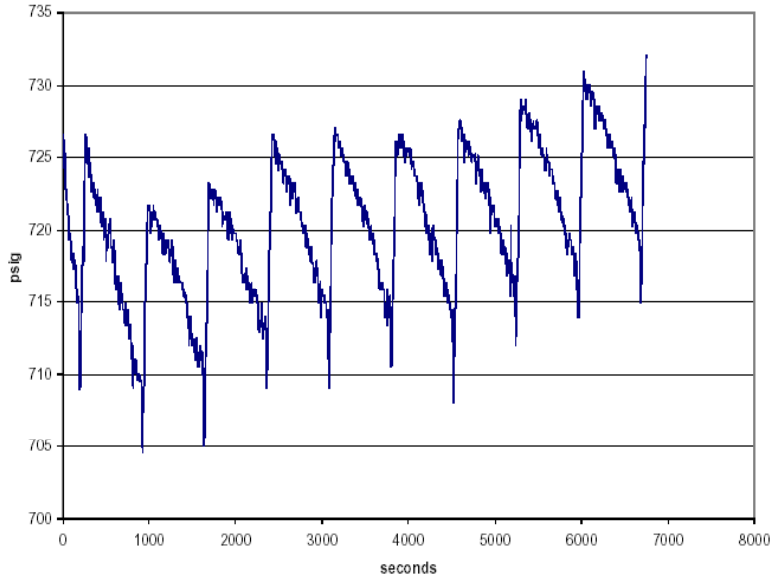

Figure 3.1: Pressure at inlet during water injection. Constant water flow rate at 14 ml/min (Habana, 2002).

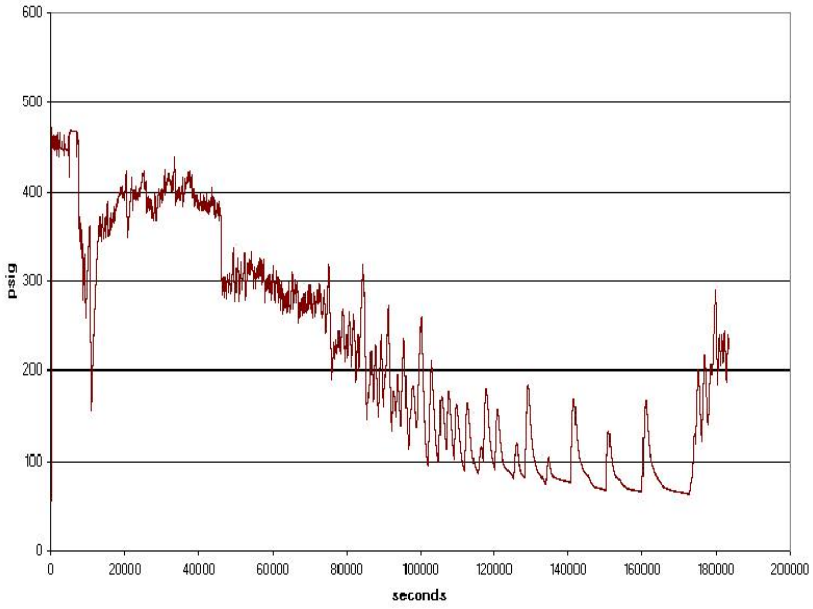

Figure 3.2: Pressure at inlet for constant flow rate nitrogen-water experiment (Habana, 2002).

3.2 EXPERIMENTAL METHODOLOGY

The rock permeability will be measured using nitrogen gas at room temperature. Gas permeability is a function of pressure. Therefore, the flow measurements will be conducted at a series of different mean pressures and taking into account Klinkenberg slip effect.

A new core sample has been obtained from a depth of 2440.5m at The Geysers geothermal field. The core is 8.9 cm in length and 4 inches in diameter.

Nitrogen will be flowed into the core at different confining pressures. Confining pressure from 500 to 850 psig can be reached by injecting nitrogen around the heat shrink tubing inside the core holder. To apply higher confining pressure water can be used in place of nitrogen.

A schematic illustration of the experiment is shown in Figure 3.3. This apparatus is now under reconstruction.

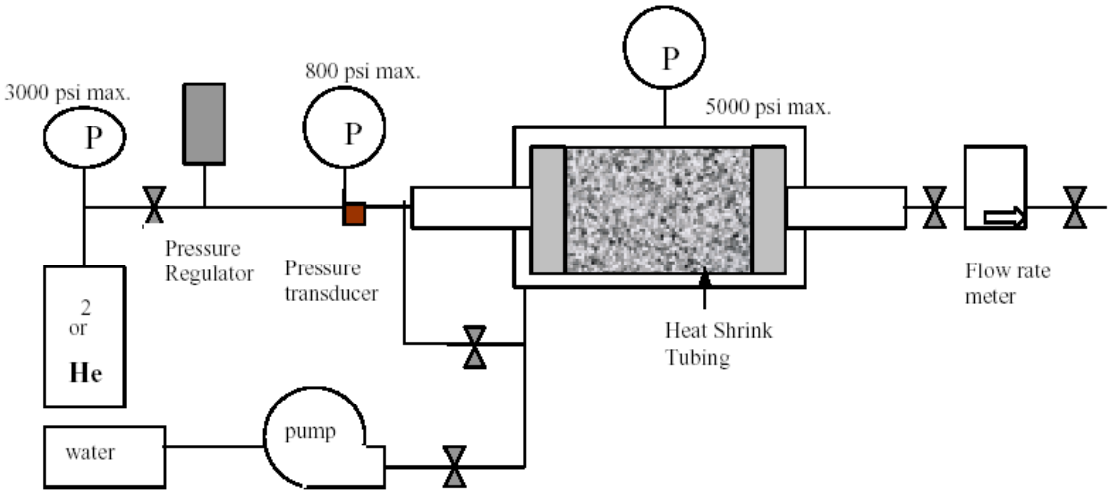

Figure 3.3: Schematic representation of apparatus

3.3 CONTINUING AND FUTURE WORK

The apparatus to be used was initially simplified and safety installations were added. Pressure transducer calibrations were also completed.

The apparatus used was also found to have a leak, which may have been the cause of the pressure spikes in the experiments of Habana (2002). The core holder was disassembled and a new core sample was prepared. The core will be dried and pore volume calculated. Further improvements to the equipment will also be made if found necessary.

Nitrogen experiments will be done after reassembling of the equipment. Water injection experiment will also be performed. After these, the apparatus will be further modified for steam-water relative permeability measurements.

4. DECLINE CURVE ANALYSIS METHOD APPLIED TO THE GEYSERS

This research project is being conducted by Research Assistant Jericho Reyes, Senior Research Engineer Kewen Li and Professor Roland Horne. The objective of this project was to develop a decline curve analysis model based on the theory of fluid flow mechanisms with relative permeability and capillary pressure included. The model reveals a linear relationship between the production rate and the reciprocal of the cumulative production. The model was applied to the production data of 61 production wells in The Geysers geothermal field and a linear relationship was found between the production rate and the reciprocal of the accumulative production for the wells, especially at the late period of production. Comparison with common methods to estimate reservoir reserves indicates that the new method gives a more definite estimate of reservoir behavior. The method can also calculate two constants obtained from the linear relationship that have physical significance and can be used to characterize the regional geological properties of the reservoir.

4.1 INTRODUCTION

Estimating reserves and predicting production performance in geothermal and petroleum reservoirs is an important but difficult task for reservoir engineers. Many papers regarding decline curve analysis methods (Chen and Teufel, 2000; Faulder, 1997; Fetkovich, 1980; Fraim and Wattenbarger, 1987; Palacio and Blasingame, 1993 and Rodriguez and Cinco-Ley, 1993) have been published. However most of the existing decline curve analysis approaches are based on the empirical exponential, hyperbolic, and harmonic equations suggested by Arps (1945). Each approach has some disadvantages. For example, the exponential decline curve tends to underestimate reserves and production rates; the harmonic decline curve has a tendency to overpredict the reservoir performance. This is not surprising for empirical techniques.

One common method to evaluate well behavior is the flow rate decline curve analysis. Sanyal et al. (1991) describes a systematic approach to this analysis by developing a method to estimate the static pressures, as well as correct the fluctuations of the wellhead pressure to correctly reflect the true decline in productivity. The methods used in the approach still uses the empirical techniques, i.e. either the harmonic or exponential decline curves. The main problem with this is that we do not know exactly which method to adopt to describe the production trend correctly.

We previously developed a model to characterize the spontaneous water imbibition into gas-saturated rocks (see Li and Horne, 2001a). The model reveals a linear relationship between the imbibition (production) rate and the reciprocal of the gas recovery (cumulative production). Although this model was derived for spontaneous water imbibition, according to our derivation it is suitable for gravity drainage or other displacement process if a piston-like saturation change is assumed. In this study, we used this model to analyze the production performance of The Geysers geothermal field.

The objectives of this study include developing a decline curve analysis method based on analytical models, and applying this to the Geysers. The study also aims to compare the results to the existing decline curve methods. Since the model is based on fluid flow mechanisms, it also aims to interpret the physical significance of the parameters derived from the analysis. Finally, the study aims to compare the results to existing empirical techniques that forecast well behavior.

4.2 THEORY

Li and Horne (2001) developed an analytical method derived from the observed linear relationship between the production rate and the reciprocal of the recovery, especially in the late period of production. The mathematical model developed previously to characterize the spontaneous water imbibition into gas-saturated rocks was the basis of this method. The model is expressed as follows:

$$q_w = a\frac{1}{R} - b \tag{4.1}$$

where q_w is the water imbibition rate; R is the recovery in terms of pore volume. a and b are two constants associated with capillary and gravity forces respectively. The details on deriving Eq. 4.1 and calculating a and b are described in Li and Horne (2001).

We can extend this model to geothermal reservoirs. Constant a is expressed as follows:

$$a = \frac{Ak_w(S_{wf} - S_{wi})}{\mu_w L} P_c \tag{4.2}$$

where A and L are the cross-section area and the characteristic height of the matrix respectively, μ_w is the viscosity of water, S_{wi} is the initial water saturation and S_{wf} is the water saturation behind the interface of steam-water; k_w is the effective permeability of the water phase at S_{wf}. Similarly, P_c is the capillary pressure at S_{wf}. Constant b is expressed as follows:

$$b = \frac{Ak_w}{\mu_w}\Delta\rho g \tag{4.3}$$

where $\Delta\rho$ is the density difference between water and steam and g is the gravity constant.

Eq. 4.1 could be expressed as follows in terms of cumulative steam production instead of recovery:

$$q_s = a_v\frac{1}{N_p} - b \tag{4.4}$$

where q_s is the steam production rate and N_p is the accumulative steam production. a_v is defined as follows:

$$a_v = aV_p \tag{4.5}$$

here V_p is the pore volume controlled by the production well or the reservoir.

The maximum cumulative steam production may be estimated by setting the steam production rate to zero or an economic limit once the linear relationship between the steam production rate and the reciprocal of the accumulative steam production is obtained. Then the reserve volume controlled by this well can be calculated, which is equal to a_v/b according to Eq. 4.4.

4.3 METHOD

We applied this method to data from The Geysers geothermal field. The Geysers production database was made available by the California Division of Oil, Gas and Geothermal Resources. The Geysers database contains production data for 502 wells around The Geysers field area. As an illustrative example, this report will describe two wells from The Geysers database, namely McKinley 1 and Thorne 1, located in the Lake and Sonoma Counties. McKinley 1, a redrilled active producer well owned by the Calpine Geysers Company, has a depth of 2219.18 feet. Thorne 1, also an active producer well, has a depth of 6842 feet. Figures 4.1 and 4.2 show the steam production flowrate history for McKinley 1 and Thorne 1 wells.

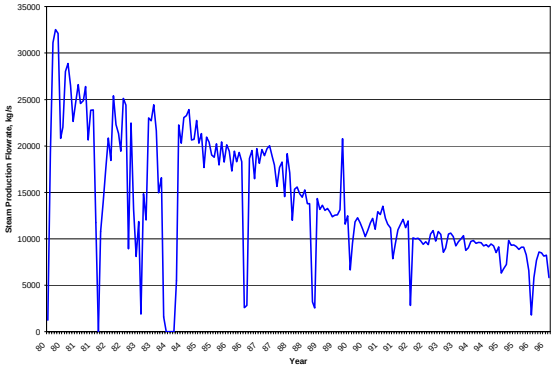

Figure 4.1: Steam production rate history of McKinley 1.

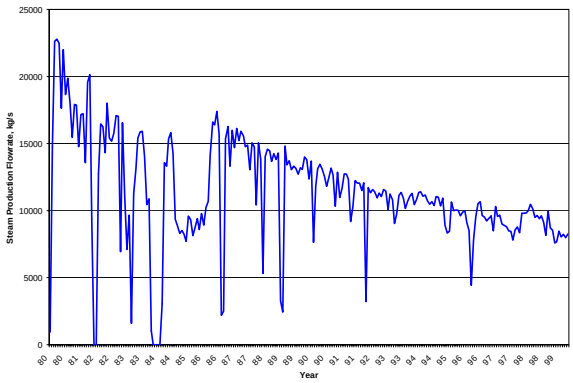

Figure 4.2: Steam production rate history of Thorne 1.

The production data for the wells correspond to various values of flowing wellhead pressure, it is therefore difficult to decipher the true decline trend without normalizing the flow rates with the standard flowing pressure, p_f. Sanyal et al. (1991) accomplished this normalization using:

$$W_n = \frac{\left(p^2 - {p_{std}}^2\right)}{\left(p^2 - {p_f}^2\right)} W \tag{4.6}$$

where W_n is the normalized production rate, p_{std} is the standard flowing wellhead pressure, W is the production rate, and p is the static pressure, which can be calculated as:

$$p^2 = \left(\frac{W}{C}\right)^{1/n} + {p_f}^2 \tag{4.7}$$

where C is an empirical parameter (Energy Resources Conservation Board, 1975), and n is the turbulence factor lying between 0.5 to 1.0. If C is assumed to be constant, its value can be approximated using:

$$C_i = \frac{W_i}{\left({p_i}^2 - {p_{fi}}^2\right)^n} \tag{4.8}$$

by taking a statistically representative value of C_i, based on the first few months of production of a well.

We plot the steam production rate with the reciprocal of the cumulative production in Figures 4.3 and 4.4 for McKinley 1 and Thorne 1. These plots show the original production rates with the normalized production rates, substituting n values for 1 and 0.5.

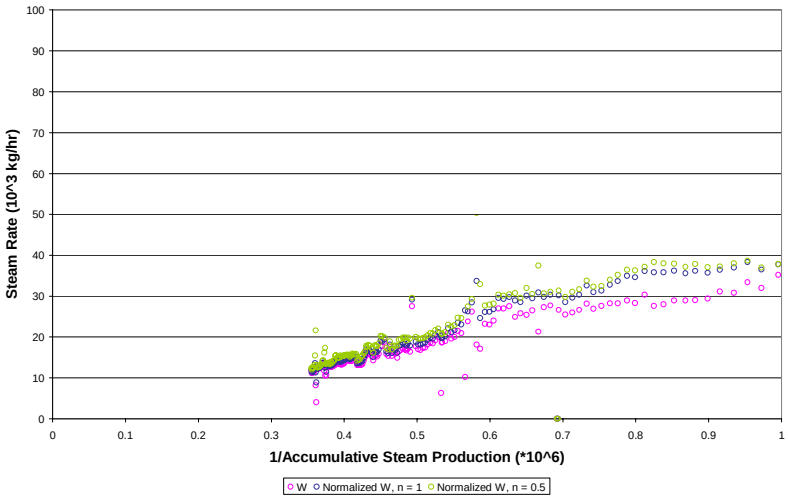

Figure 4.3: Relationship between the steam production rate and the reciprocal of the cumulative steam production for McKinley 1 using the original and normalized production rates with n = 0.5 and 1.

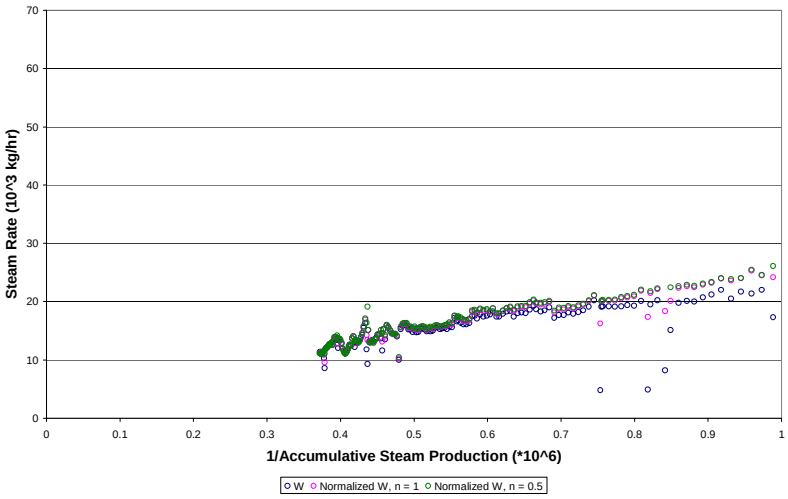

Figure 4.4: Relationship between the steam production rate and the reciprocal of the cumulative steam production for Thorne 1 using the original and normalized production rates with n = 0.5 and 1.

We see from these figures that normalization produces a significant reduction in the fluctuations of the rates, and the choice of n value has little affect on the W_n calculated. We chose $n = 1$ for further calculations.

At late time, the plots in Figures 4.3 and 4.4 show the relationship between the steam production rate and the reciprocal of the cumulative steam production. The relationship is closely linear, so the two constants a_v and b could be calculated using the linear model represented by Eq. 4.

Since the fluid flow mechanism Eq. 4.4 is based on two-phase fluid flow, we need to identify at which point the production history is based on two-phase flow. Reyes (2003) explored the historical production data of the Geysers in detail and one of the findings was that the majority of the wells at around 1991 – 1992. A method was developed to identify this point. We took the 177 wells that had this dry-out point and applied the decline curve method discussed in this study. Figures 4.5 and 4.6 show the linear trend suggested by Eq. 4.4 at a late time period for McKinley 1 and Thorne 1 well production histories. We also identify in these figures where the dry-out point is, which is essentially where the linear trend ends.

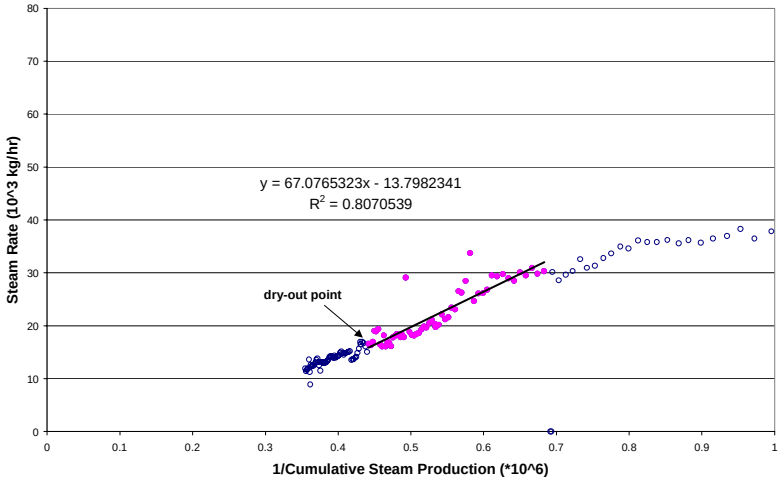

Figure 4.5: Relationship between the steam production rate and the reciprocal of the accumulative steam production for McKinley 1.

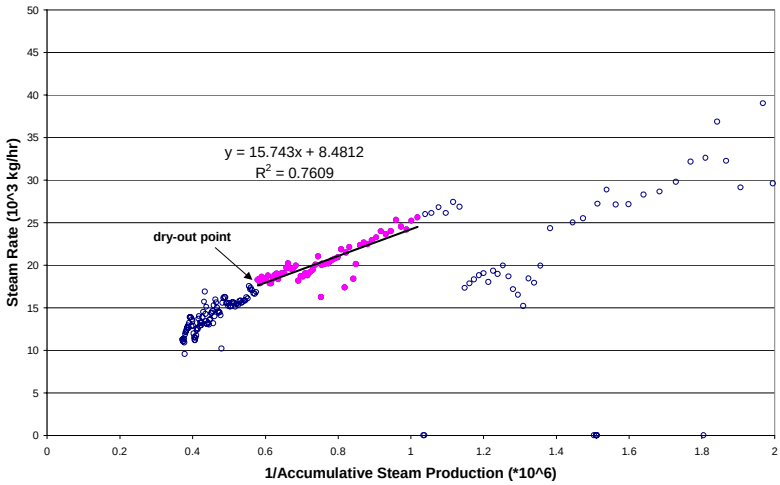

Figure 4.6: Relationship between the steam production rate and the reciprocal of the accumulative steam production for Thorne 1.

We compared the decline curve method developed so far to the existing empirical decline curve analysis methods. We discuss these methods here in brief.

Harmonic decline is defined by:

$$-\frac{1}{W}\frac{dW}{dt} = D(t) \tag{4.9}$$

where t is the time in years and $D(t)$ is the decline rate in years. The harmonic trend rate at any instant is directly proportional to the productivity at that instant.

Exponential decline is defined by:

$$-\frac{1}{W}\frac{dW}{dt} = D \tag{4.10}$$

where D is the constant decline rate.

If the decline trend is exponential, one should get a linear trend by plotting the logarithm of W versus time. If the decline trend is harmonic, we expect a linear trend by plotting W versus. We therefore make plots for both methods, with time plotted as cumulative production. Figures 4.7 and 4.8 are the harmonic plots for McKinley 1 and Thorne 1, respectively, and Figures 4.9 and 4.10 are exponential plots for McKinley 1 and Thorne 1. We also fit the linear decline trends that these methods predict.

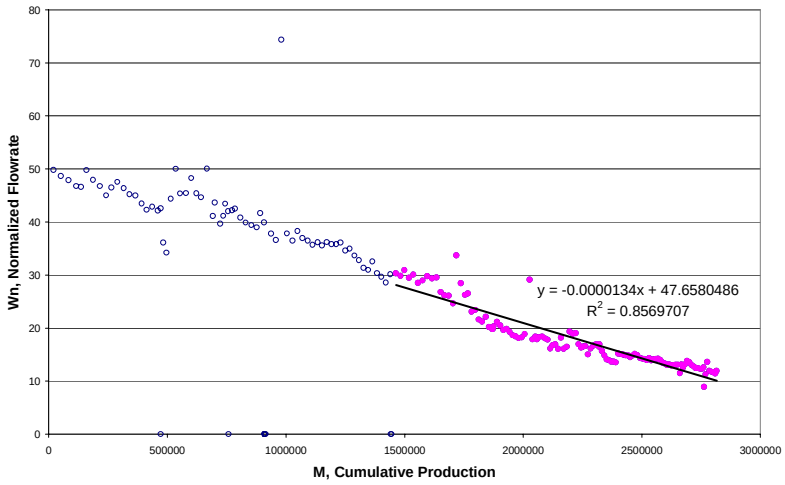

Figure 4.7: Harmonic decline curve analysis for McKinley 1.

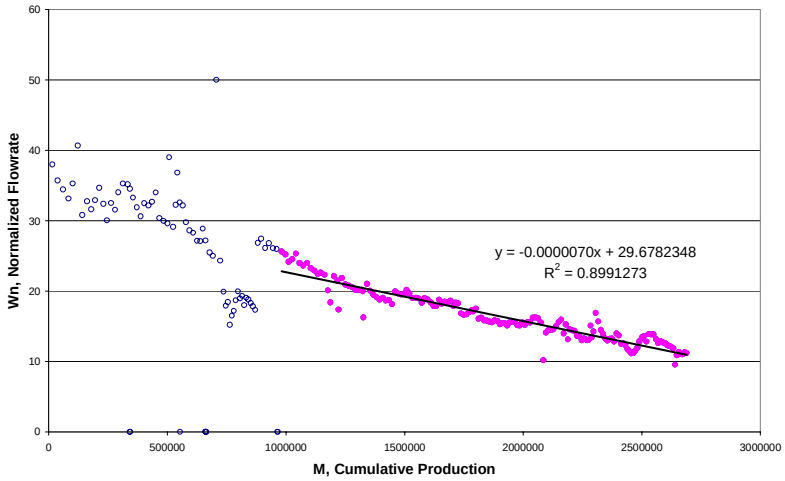

Figure 4.8: Harmonic decline curve analysis for Thorne 1.

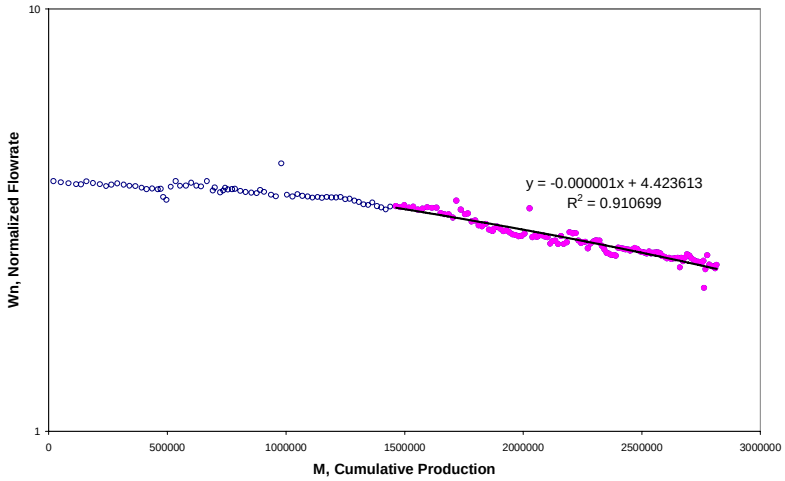

Figure 4.9: Exponential decline curve analysis for McKinley 1.

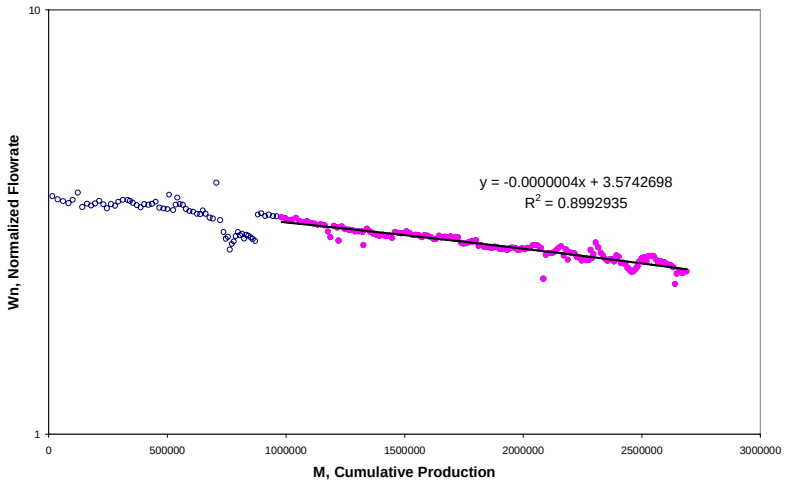

Figure 4.10: Exponential decline curve analysis for Thorne 1.

We can therefore compare these three methods by calculating cumulative production values from the fitted linear trends.

4.4 RESULTS

The product of the effective permeability of the water phase and the area controlled by the production well may be evaluated according to Eq. 4.3 using the value of constant *b*. The maximum cumulative steam production N_{pmax} can also be estimated once the values of the two constants a_v and *b* are available ($N_{pmax} = a_v/b$). Figures 4.5 and 4.6 fitted linear trends based on the relationship presented in Eq. 4.4. To facilitate the calculation of N_{pmax}, we need negative values for the constant *b* to have a positive value for N_{pmax}. We observe 61 wells out of 177 that show this trend, as the rest of the wells do not have the suitable linear decline trends to estimate the cumulative steam production. Table 4.1 shows the values a_v, *b*, and N_{pmax} for the 61 wells.

Table 4.1: Values of a_v, b, and N_{pmax} for 61 wells at the Geysers.

Well Name	a_v	b	N_{pmax}
Abel 1	124.89	1.3179	10552486
Beigel 2	114.98	24.679	2146373
Beigel 3	177	40.134	2267458
CA-5634 21-12	252.6	164.02	6493270
CA-5636 68B-21	231.42	39.865	17226255
CA-5636 87C-21	142.3	16.769	11784259
CA-5636 87D-21	118.96	17.037	14321621
CA-5637 68-21	162.87	24.097	14795235
CA-5639 15D-28	1.7388	22.614	13005521
CA-5639 44-28	1143.1	410.61	3592074
CA-5639 44B-28	505.95	153.13	3026584
CA-5639 53-33	96.492	87.801	9099304
CA-5639 63-29	27.006	4.131	1529660

CA-5639 63A-29	150.8	47.554	3153448
CA-5639 85-28	45.048	110.34	2449387
CA-958 37-34	217.13	47.15	2171510
CA-958 37A-34	1034.4	139.7	13505414
CA-958 37C-34	11.869	103.92	8755582
CA-958 56B-34	53.173	2.1445	4033062
D & V 1	106.31	8.3701	7873295
D & V 12	362.71	23.806	6563370
D & V 2	62.403	4.3597	6986363
D & V 6	106.98	185.41	1733128
D & V A-2	180.61	3.4866	19304579
D & V A-4	5.511	44.813	8131555
DX State 4596 25	4.3668	24.272	5558304
DX State 4596 50	96.168	7.7706	8080235
DX State 4596 60	174.05	2.2221	12767021
DX State 4596 74	249.86	116.02	4643400
DX State 4596 82	34.36	74.882	2179336
GDC 1	31.628	17.082	5400911
GDC 10	865.4	107.73	12448579
GDC 11	385.37	58.459	15169577
GDC 19	571.32	432.29	7566513
GDC 2	116.44	36.352	3121951
GDC 20-29	23.563	31.075	13188049
GDC 23	1103.6	488.12	4422979
GDC 24	130.73	506.11	3871414
GDC 7	252.54	34.341	13598242
LF State 4597 1	78.321	16.879	2155105
LF State 4597 13	73.992	5.3874	7281057
LF State 4597 29	148.48	21.703	14616783
LF State 4597 31	108.97	14.698	13488116
LF State 4597 36	89.406	14.875	1663759
LF State 4597 42	38.882	64.02	1646520
LF State 4597 5	163.22	10.347	6339297
McKinley 1	45.363	2.9425	6486564
McKinley 10	335.6	47.759	14230930
McKinley 3	96.735	0.4107	4245619
McKinley 9	112.83	8.645	7661969
MLM 2	83.772	5.7483	6861839
Modini 1	102.79	4.7799	4650161
Modini 3	164.37	15.889	9666606
Modini 4	362.06	23.432	6471855
Ot St 4596 16	53.325	0.2358	4421941
Ot St 4596 29	5.7716	39.769	6890464
Sulphr Bank 10	6.2969	24.7	3922565
Sulphr Bank 20	115.46	6.2601	54218777
Sulphr Bank 21	68.766	0.2717	3951080
Sulphr Bank 26	74.59	3.9897	5348840
Tocher 3	64.679	22.422	3466658

We performed a similar calculation for N_{pmax} using harmonic and exponential decline analysis and made a comparison with the developed method. We summarize this comparison in Figure 4.11. In this figure, we also plot the corresponding in-situ water saturation, which was inferred in Reyes (2003).

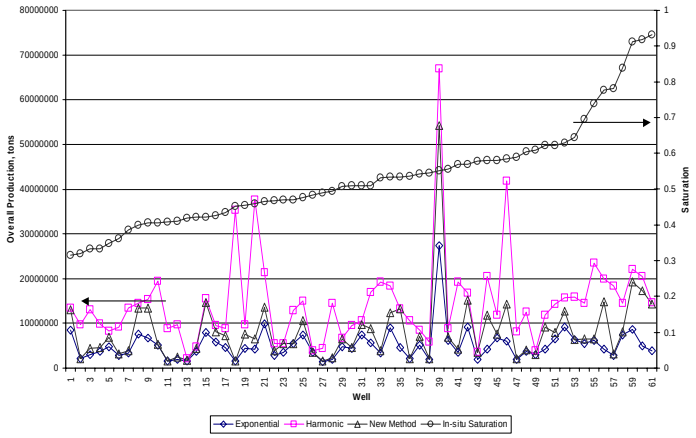

Figure 4.11: Comparison of the calculated N_{pmax} *values between the decline curve methods with the in-situ water saturation (Reyes, 2003).*

Figure 4.11 shows us that almost all of the N_{pmax} values calculated from the new decline curve method lie between the exponential and harmonic N_{pmax} values. Since exponential analysis often underestimate the reserves, and harmonic analysis often overestimates the reserves, we can say that the method gives a more suitable estimation. A more accurate snapshot of the reserves in geothermal wells is crucial in the development strategies often undertaken in geothermal power plants. It is also observed that the trend of increasing value of the inferred in-situ water saturation plotted is not reflected in the cumulative production values for any of the three methods.

Another facet of the new decline curve method is the calculation of a_v and b, which implies that these wells may have similar recoverable reserves and reservoir properties. This phenomenon may be related to the region and the geology. We map these two constants with respect to their location in the Geysers map, and Figures 4.12 and 4.13 shows the spatial relationships of these two constants.

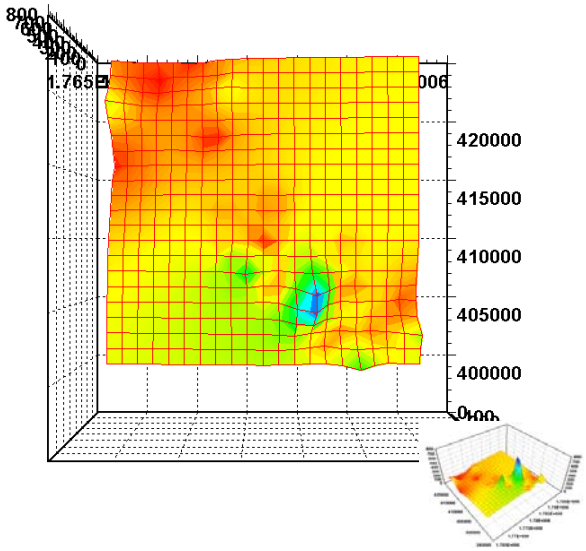

Figure 4.12: Aerial view contour plot of the imbibition index (a_v) values on the Cartesian plane of 61 Geyser wells (inset: 3D view).

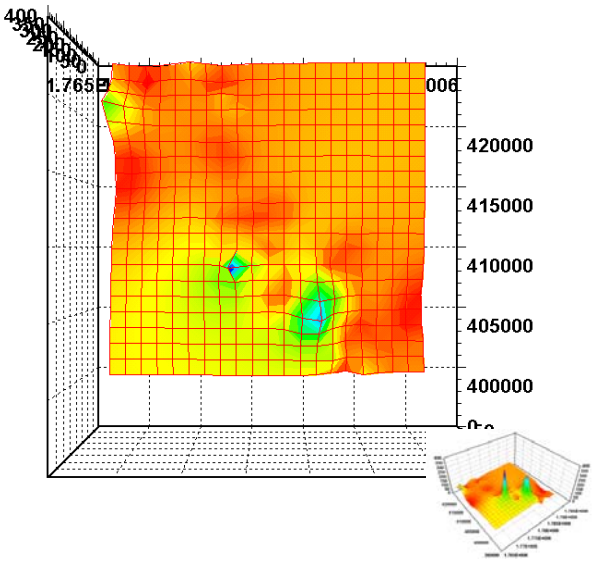

Figure 4.13: Aerial view contour plot of the gravity force constant (b) on the Cartesian plane of 61 Geyser wells (inset: 3D view).

We see from the figures that generally we see similar values a_v and b, which implies that these wells may have similar recoverable reserves and reservoir properties, except for two spots in particular with larger values. Li and Horne (2003) refers to a_v as the imbibition index because it representative of the recovery rate by spontaneous imbibition. Greater values of a_v suggest faster imbibition. The constant b corresponds to the gravity forces. Larger values suggest differing geological properties in these two spots, compared to the rest of the field.

It is interesting to note that near these two spots, there are two significant injection wells present, McKinley 5 and MLM 1. These two wells contribute more injection water than the other 23 wells identified with injection records in the 503 wells surveyed. Also present in these spots are other injection wells such as CA-1862 21-28 and Davies Estate 1.

4.5 DISCUSSION

From Figure 4.11, there is no apparent relationship between the in-situ water saturation that were inferred in the Reyes (2003) study and the decline curve indices. A possible explanation for this is that the pore volumes that the individual wells drain for their production differ in each well. Other factors that may explain the discrepancy could be the varying field properties like permeability or porosity that may differ from well to well.

The development of a decline curve analysis method that is based on fluid flow mechanisms is very useful, especially if the uncertainty of choosing between the present methods is crucial to the economic viability of the project. Also, the knowledge of other factors that might affect the decline curve properties of the data, i.e. transition from multiphase to single-phase production, can be taken into account in this model. It is especially useful for geothermal reservoirs, where phase transitions is more apparent than that in oil-gas systems.

The presence of significant injection wells near the zones of large values of a_v and b indicate that this is an alternative way to determine where to inject in a geothermal reservoir. Since reinjection schemes are often subject to comprehensive studies that include observing significant decreases in reservoir pressure, among others, knowing values of a_v and b can be another way to determine if a certain region in a geothermal reservoir is a prime spot for reinjection. Since a_v and b pertain to the imbibition index and gravity forces, respectively, these two parameters are critical to the effectiveness of any reinjection strategy. Higher imbibition indices that correspond to higher imbibition rates, and higher gravity force numbers mean that reinjection will be undertaken in a more efficient way.

Also, to aid with present reinjection strategies in geothermal reservoirs, with the knowledge of both properties, we can make decisions on whether changing both properties will enhance our reinjection scheme, especially if the values are equal to or lower than the average found in the field.

Eq. 4.4 was derived for a simple linear fluid flow. Due to the complexity of reservoir conditions, it may be necessary to modify Eq. 4.4 by considering heterogeneity, fracture density, compressibility, boundary conditions, radial flow, and other factors.

4.6 CONCLUSIONS

Based on the present study, the following conclusions may be drawn:

1. An analytical decline curve analysis model was developed based on the theory of fluid flow in porous media and was verified using the production data from the geothermal reservoirs at The Geysers.
2. The relationship between the production rate and the reciprocal of the cumulative production is linear and may be used to estimate reservoir properties and recoverable reserves.
3. There is no apparent relationship between the inferred in-situ water saturation (Reyes, 2003), and the cumulative production values found in the decline curve methods.
4. The decline curve analysis method based on fluid flow mechanisms gives us a definite estimate of reservoir behavior, compared to the choice faced in using empirical methods.
5. Physical parameters derived from the decline curve analysis discussed can be used to describe regional and reservoir properties and can be used in practical ways such as to design reinjection strategies.

5. REFERENCES

Abdassah, D., Permadi, P., and Sumantri, R.: “Saturation Exponents Derived from Fractal Modeling of Thin Sections,” SPE 36978, presented at the 1996 SPE Asia Pacific Oil and Gas Conference held in Adelaide, Australia, October 28-31-17, 1996.

Angulo, R.F. and Gonzalez, H.: “Fractal Dimensions from Mercury Intrusion Capillary Tests,” SPE 23695, presented at the 2nd Latin American Petroleum Engineering Conf. of SPE held in Caracas, Venezuela, March 8-11, 1992.

Arps, J.J.: "Analysis of Decline Curves," *Trans*. AIME (Dec. 1945) 160, 228-247.

Brooks, R.H. and Corey, A.T.: “Hydraulic Properties of Porous Media,” Colorado State University, Hydro paper No.5 (1964).

Brooks, R. H. and Corey, A. T.: "Properties of Porous Media Affecting Fluid Flow", *J. Irrig. Drain. Div*., (1966), 6, 61.

Chen, C.-Y., Diomampo, G., Li, K. and Horne, R.N.: "Steam-Water Relative Permeability in Fractures," *Geothermal Resources Council Transactions Vol.26*, pp. 87-94, 2002.

Chen, H.Y. and Teufel, L.W.: “A New Rate-Time Type Curve for Analysis of Tight-Gas Linear and Radial Flows,” paper SPE 63094, presented at the 2000 SPE Annual Technical Conference and Exhibition, Dallas, TX, October 1-4, 2000.

Corey, A. T.: "The Interrelation between Gas and Oil Relative Permeabilities", *Prod. Mon*., (1954), **19**, 38.

Cuttler, W.W. Jr.: "Estimation of Underground Oil Reserves by Oil-Well Production Curves," *Bull*., USBM (1924) 228.

Diomampo, G., "Relative Permeability through Fractures", MS thesis, Stanford University, Stanford, California (2001).

Faulder, D.D.: “Advanced Decline Curve Analysis in Vapor-Dominated Geothermal Reservoirs,” paper SPE 38763, presented at the 1997 SPE Annual Technical Conference and Exhibition, San Antonio, TX, October 5-8, 1997.

Fetkovich, M.J.: "Decline Curve Analysis Using Type Curves," *JPT* (June. 1980) 1065-1077.

Fourar, M. and Bories, S.,: "Experimental Study of Air-Water Two-Phase Flow Through A Fracture (Narrow Channel)," *Int. J. Multiphase Flow* Vol. 21, No. 4, (1995) pp. 621-637.

Fourar, M., and Lenormand, R.,: "A Viscous Coupling Model for Relative Permeabilities in Fractures," Paper SPE 49006, Presented at the SPE Annual Technical Conference and Exhibition, New Orleans, Louisiana, USA, September 27-30, 1998.

Fraim, M.L. and Wattenbarger, R.A.: "Gas Reservoir Decline Analysis Using Type Curves With Real Gas Pseudopressure and Normalized Time," *SPEFE* (December 1987).

Friesen, W.I. and Mikula, R.J.: “Fractal Dimensions of Coal Particles”, *J. of Colloid and Interface Science*, **120**(1), 263-271 (November 1987).

Habana, M.D.: "Relative Permeability of Fractured Rock", MS report, Stanford University, Stanford, California, (2002).

Hansen, J.P. and Skjeltorp, A.T.: “Fractal Pore Space and Rock Permeability Implications,” *Phys. Rev.* B, **38**(4), 2635-2638 (1988).

Horne, R.H., Satik, C., Mahiya, G., Li, K., Ambusso, W., Tovar, R., Wang, C., and Nassori, H.: "Steam-Water Relative Permeability," Proc. of the World Geothermal Congress 2000, Kyushu-Tohoku, Japan, May 28-June 10, 2000.

Katz, A.J. and Thompson, A.H.: “Fractal Sandstone Pores: Implications for Conductivity and Pore Formation,” *Phys. Rev. Lett.*, **54**, 1325-1328 (1985).

Krohn, C.E.: “Fractal Measurements of Sandstones, Shales, and Carbonates,” *J. of Geophysical Research*, **93**(B4), 3297-3305 (1988).

Lenormand, R.: “Gravity-Assisted Inert Gas Injection: Micromodel Experiments and Model Based on Fractal Roughness,” The European Oil and Gas Conference, Altavilla Milica, Palermo, Sicily, October 9-12, 1990.

Li, K. and Horne, R.N. (2000a): “Steam-Water Capillary Pressure,” SPE 63224, presented at the 2000 SPE Annual Technical Conference and Exhibition, Dallas, TX, USA, October 1-4, 2000.

Li, K., Nassori, H., and Horne, R.N. (2001): “Experimental Study of Water Injection into Geothermal Reservoirs,” to be presented at the GRC 2001 annual meeting, August 26-29, 2001, San Diego, USA; *GRC* Trans. V. **25**.

Li, K. and Horne, R.N. (2001a): “Characterization of Spontaneous Water Imbibition into Gas-Saturated Rocks,” *SPEJ* (December 2001), p62-69.

Li, K. and Horne, R. N. (2001b): Quarterly Report for October-December 2001, Stanford Geothermal Program, DE-FG07-95ID13763.

Li, K. and Horne, R.N.: “Fractal Characterization of The Geysers Rock,” presented at the GRC 2003 annual meeting, October 12-15, 2003, Morelia, Mexico; GRC *Trans*. **27** (2003).

Mahiya, G.: “Experimental Measurement of Steam-Water Relative Permeability,” MS report, Stanford University, Stanford, California (1999).

Mendoza, C.A. and Sudicky, E.A.,: "Hierarchical Scaling of Constitutive Relationships Controlling Multi-phase Flow in Fractured Geologic Media," paper presented at the Third Int. Conf. on Reservoir Characterization Requirements for Different Stages of Development, Tulsa, OK, 1991.

Moulu, J-C., Vizika, O., Kalaydjian, F., and Duquerroix, J-P.: “A New Model for Three-Phase Relative Permeabilities Based on a Fractal Representation of the Porous

Media," SPE 38891, presented at the SPE Annual Technical Conference and Exhibition, San Antonio, TX, USA, October 5-8, 1997.

Murphy, J.R. and Thomson, N.R.,: "Two-Phase Flow in a Variable Aperture," *Water Resources Research*, vol. 29, No 10, pp. 3453-3476, 1993.

O'Connor, P.A.: "Constant-Pressure Measurement of Steam-Water Relative Permeability," MS report, Stanford University, Stanford, California (2001).

Palacio, J.C. and Blasingame, T.A.: "Decline Curve Analysis Using Type Curves: Analysis of Gas Well Production Data," paper SPE 25909 presented at the 1993 SPE Rocky Mountain Regional/Low Permeability Reservoirs Symposium, Denver, CO, April 12-14.

Pan, X., Wong, R.C., and Maini, B.B.,: "Steady State Two-Phase Flow in a Smooth Parallel Fracture," presented at the 47th Annual Technical Meeting of the Petroleum Society in Calgary, Alberta, Canada, June 10-12, 1996.

Pérez Bernal, J.L. and Bello López, M.A.: "The Fractal Dimension of Stone Pore Surface as Weathering Descriptor," *Applied Surface Science*, **161**, 47-53 (2000).

Persoff, P. K., Pruess, K., and Myer, L.: "Two-Phase Flow Visualization and Relative Permeability Measurement in Transparent Replicas of Rough-Walled Rock Fractures," *Proc. 16th Workshop on Geothermal Reservoir Engineering*, Stanford University, Stanford, California, January 23-25, 1991.

Persoff, P., and Pruess, K.: "Two-Phase Flow Visualization and Relative Permeability Measurement in Natural Rough-Walled Rock Fractures," *Water Resources Research* Vol. 31, No. 5, May, 1995, pp. 1175-1186.

Purcell, W.R.: "Capillary Pressures-Their Measurement Using Mercury and the Calculation of Permeability", *Trans. AIME*, (1949), **186**, 39.

Pyrak-Nolte, L.J., Helgeston, D., Haley, G.M., and Morris, J.W.,: "Immiscible Fluids Flow in Fracture," *Proceeding of the 33rd U.S. Rock Mech. Symp.*, edited by Tillersson and Wawersik, pp. 571-578, A. A. Balkema, Rotterdam, Netherlands, 1992.

Reyes, J.L.P., "Estimating In-situ Water Saturation at The Geysers Based on Historical Pressure and Temperature Production Data and by Direct Measurement", MS thesis, Stanford University, Stanford, California (2003).

Rodriguez, F. and Cinco-Ley, H.: "A New Model for Production Decline," paper SPE 25480 presented at the Production Operations Symposium, Oklahoma City, OK, March 21-23, 1993.

Romm, E.S.: "Fluid Flow in Fractured Rocks", "Nedra" Publishing House, Moscow, 1966 (Translated from the Russian).

Rossen, W.R., and Kumar A.T.A.,: "Single and Two-phase Flow in Natural Fractures," SPE 24195, the 67th SPE Annual Technical Conference and Exhibition, Washington D.C., Oct. 4-7, 1992.

Sanyal, S.K., Menzies, A. J., Brown, P.J., Enedy, K.L. and Enedy, S.L.: "A Systematic Approach to decline Curve Analysis for the Geysers Steam Field, California," Monograph on The Geysers Geothermal Field, Special Report No. 17, pp. 189 – 192. 1992.

Satik, C.: "A Measurement of Steam-Water Relative Permeability," Proceedings of 23rd Workshop on Geothermal Reservoir Engineering, Stanford University, Stanford, California (1998).

Scheidegger, A.E. *The Physics of Flow Through Porous Media*, 3rd ed., University of Toronto, Toronto. 1974.

Shen, P. and Li, K.: "A New Method for Determining the Fractal Dimension of Pore Structures and Its Application," Proceedings of the 10th Offshore South East Asia Conference, Singapore, December 6-9, 1994.

Shen, P. and Li, K.: "Quantitative Description for the Heterogeneity of Pore Structure by Using Mercury Capillary Pressure Curves," SPE 29996, Proceedings of the SPE International Meeting held in Beijing, China, November 14-17, 1995.

Toledo, P.G., Novy, R.A., Davis, H.T., and Scriven, L.E.: "Capillary Pressure, Water Relative Permeability, Electrical Conductivity and Capillary Dispersion Coefficient of Fractal Porous Media at Low Wetting Phase Saturations" *SPE Advanced Technology Series* (1993), **2**(1), 136-141.

Witherspoon, P.A., Wang, J.S.W., Iwai, K. and Gale, J.E.: " Validity of Cubic Law for Fluid Flow in a Deformable Rock Fracture," *Water Resources Research*, Vol. 16, No. 6, 1980, pp 1016-1024.

Wong, P., Howard, J., and Lin, J. S.: "Surface Roughening and the Fractal Nature of Rocks," *Phys. Rev. Lett.*, **57**, 637-640 (1986).

Yih, C.S., *Fluid Mechanics*, McGraw-Hill, New York. 1969.